JETP Letters, Vol. 79, No. 8, 2004, pp. 361–364. Translated from Pis'ma v Zhurnal Éksperimental'noĭ i Teoreticheskoĭ Fiziki, Vol. 79, No. 8, 2004, pp. 443–447.

On the Possibility of Terahertz Wave Generation upon Dense Gas Optical Breakdown

S. V. Golubev, E. V. Suvorov, and A. G. Shalashov*

Institute of Applied Physics, Russian Academy of Sciences, ul. Ul'yanova 46, Nizhni Novgorod, 603950 Russia

**e-mail: ags@appl.sci-nnov.ru*

Received March 2, 2004; in final form, March 22, 2004

The possibility of applying the physical principles underlying the operation of a solid-state terahertz oscillator to plasma gas-discharge media is analyzed. A new method of electromagnetic wave generation in the terahertz frequency range is proposed. It is based on the excitation of plasma-oscillation current by a static electric field in a laser spark produced by an axicon lens, followed by the radiation of an electromagnetic pulse through the Cherenkov mechanism. © *2004 MAIK "Nauka/Interperiodica".*

PACS numbers: 42.65.Re; 41.60.Bq; 52.38.-r

1. The fabrication of efficient sources of electromagnetic radiation in the terahertz frequency range (1–50 THz) is a topical radiophysical and engineering problem. This relatively "new" type of radiation can find use in the physicochemical analysis of materials, in medicine for tissue echography and tomography, and in promising communication systems. Prototypes of semiconductor emitters, detectors, and spectrometers for the analysis of terahertz signals have now been developed [1–4]. The development in this direction is mainly associated with the design of terahertz oscillation sources based on the frequency down-conversion in ultrashort optical pulses using optoelectronic semiconductor devices. In essence, this process is a detection of an optical pulse in the case where the shape of a radiated signal is close to the envelope of a high-frequency optical pulse. This detection is accomplished using either semiconductors with a pronounced nonlinear polarization response or "fast" photoconductors with a short charge-carrier lifetime. In the latter case, the photocurrent is created by electrostatic fields (either external or internal); the crystal illumination by a pulsed laser results in the excitation of a surface current, which becomes the source of terahertz radiation.

In this work, a closely related idea based on the possibility of exciting a free-carrier current in a gaseous medium by an electric field of optical radiation is considered. In essence, we suggest that the generation mechanism operating in the aforementioned solid-state semiconductor devices can be applied to plasma media as well. The suggested method of electromagnetic wave generation in the terahertz frequency range is based on the excitation of a Langmuir-oscillation current in a laser spark plasma using an external static electric field.

The principle of operation of such a source is illustrated in the figure. An ultrashort laser pulse is focused by an axicon lens in a dense gas. It is known that the axicon focuses the incident beam into a filament extended along its axis (axicon caustic [5]). The ionization wave arising along the focusing axis propagates with the superrelativistic velocity $c' = c/\cos\vartheta_0$, where ϑ_0 is the lens focusing angle. In the presence of an external electric field, ionization is accompanied by the appearance of a plasma-polarization wave. As a result of polarization, a plasma-oscillation current wave arises. It propagates with the superrelativistic velocity and radiates an electromagnetic pulse through the Cherenkov mechanism.

2. Let us assume that the laser intensity is so high that the gas tunneling ionization proceeds much more rapidly than all other processes accompanying the terahertz generation. Consider a cylindrical region with the symmetry axis coinciding with the laser-field focusing axis (figure). We first assume that the total ionization of neutral gas proceeds *instantaneously* over the entire volume of this region. In the presence of an external static electric field, plasma oscillations are excited in this region. Assume for definiteness that the external

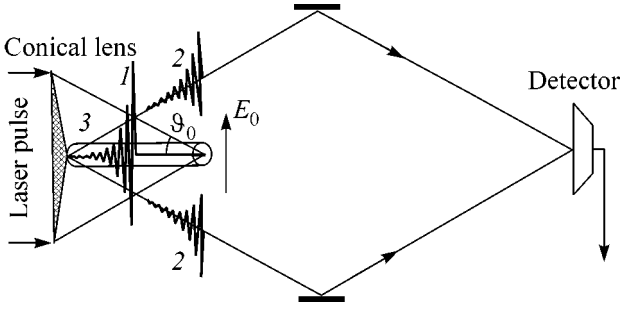

Scheme of plasma source of terahertz radiation: (*1*) current pulse; (*2*) THz pulse; (*3*) discharge zone.

0021-3640/04/7908-0361$26.00 © 2004 MAIK "Nauka/Interperiodica"

field $\mathbf{E}_0$ is orthogonal to the cylinder axis. Then, the Tonks– Dattner oscillations [6, 7] of a cylindrical plasma column are excited with frequency ω that can be found, in the approximation of "cold" plasma with the dielectric constant $\varepsilon(\omega)$, from the following dispersion relation:[1]

$$\varepsilon(\omega) = -1, \quad \varepsilon(\omega) = 1 - \frac{\omega_p^2}{\omega(\omega - i\nu_e)}. \qquad (1)$$

Here, $\omega_p = (4\pi e^2 N/m)^{1/2}$ is the plasma (Langmuir) frequency of the electronic component; $\nu_e \approx 4\pi e^4 \ln\Lambda N/m^2 v_e^3$ is the effective frequency of electron collisions (in this work, it is set equal to the transport frequency of electron–ion Coulomb collisions); N is the buffer gas concentration; and $v_e = (2T_e/m)^{1/2}$, e, and m are the electron thermal velocity, charge, and mass, respectively. Dispersion relation (1) can be regarded as the solution to the following differential equation for the electron displacement $x(t)$ with respect to the fixed ions along the electric field:

$$\ddot{x} + \nu_e \dot{x} + (\omega_p^2/2)x = -eE_0/m. \qquad (2)$$

After the instantaneous ionization at $t = 0$, damped plasma oscillations are excited. They are described by Eq. (2) with zero initial conditions for the electron displacement and velocity $x(0) = \dot{x}(0) = 0$. In particular, the solution for the current $j = -eN\dot{x}$ caused by the self-consistent electron motion in an external field and a charge-separation field can easily be found:

$$\mathbf{j}(t) = \begin{cases} \mathbf{j}_0 e^{-\nu_e t/2} \sin\omega t \text{ at } t \geq 0 \\ 0 \text{ at } t < 0, \end{cases} \quad \mathbf{j}_0 = \frac{\omega_p^2 \mathbf{E}_0}{4\pi\omega}, \qquad (3)$$

where $\omega = \sqrt{\omega_p^2/2 - \nu_e^2/4}$ is the oscillation frequency with allowance for the cylindrical symmetry and damping. Since the ionization in different regions proceeds with a time delay because of the finite pulse-phase propagation velocity along the focusing axis (z axis), the expression for the polarization-current density over the entire spark volume can be written as

$$\mathbf{j}(t, z) = \mathbf{j}(t - z/c'), \qquad (4)$$

where the right-hand side is given by Eq. (3). Here, we ignored the effects caused by the nonuniformity of laser field across the focusing axis.

The hydrodynamic description of plasma oscillations on the basis of Eqs. (1) and (2) is valid if the oscillations at every space point are mutually independent and the amplitude of these oscillations is small compared to the characteristic size of the region. The first condition implies, in fact, that the spatial dispersion of plasma waves is small; i.e., $kv_e \ll \omega_p$. The second condition can be written as $\delta x \sim eE_0/m\omega_p^2 \ll a$, where δx is the maximal electron displacement with respect to ions and a is the spark transverse size. One can readily verify that, for the atmospheric pressure of buffer gas, both conditions are fulfilled with a large margin (e.g., for the parameters presented at the end of this article).

3. The radiation from a current in vacuum can conveniently be determined through the retarded vector potential [12]:

$$\mathbf{A}(t, \mathbf{r}) = \frac{1}{c}\int \frac{\mathbf{j}(t - R/c, \mathbf{r}')}{R} d^3\mathbf{r}', \quad R = |\mathbf{r} - \mathbf{r}'|. \qquad (5)$$

In our case, the radiating volume has the form of an extended cylinder with radius a and length L ($L \gg a$); a cross-sectionally uniform current wave $\mathbf{j}(t - z/c')$ propagates along the cylinder axis. In the Fraunhofer zone ($r \gg L^2|\omega|\sin^2\vartheta/2c$ and $a < 2\pi c/\mathrm{Re}\,\omega$), one can retain only the two first terms in the expansion of R in powers of r/L: $R = r - z'\cos\vartheta + z'^2\sin^2\vartheta/2r + \ldots$, where z' is the coordinate along the cylinder axis and ϑ is the angle between the z' axis and the observation angle in the expression for the retarded potentials. As a result, the vector potential is determined by

$$\mathbf{A}(t) \approx \frac{1}{cr}\int_{-L/2}^{L/2} \mathbf{j}(t - r/c + z'\xi/c)\pi a^2 dz', \qquad (6)$$

where $\xi = \cos\vartheta - c/c'$ is the new angular variable introduced for the sake of brevity. The radiation electric field can easily be found from this expression:

$$\mathbf{E}(t) = -\frac{1}{c}\frac{\partial \mathbf{A}(t)}{\partial t}$$

$$\approx -\frac{1}{c^2 r}\int_{-L/2}^{L/2} \frac{\partial}{\partial t}\mathbf{j}(t - r/c + z'\xi/c)\pi a^2 dz' \qquad (7)$$

$$= -\frac{\pi a^2}{cr\xi}\{\mathbf{j}(t - r/c + L\xi/2c) - \mathbf{j}(t - r/c - L\xi/2c)\}.$$

This expression describes the Cherenkov radiation with a radiation pattern having a maximum at the angle ϑ_0 to the focusing axis of laser pulse (recall that $\cos\vartheta_0 = c/c'$ is determined from the focusing angle of the laser beam). The width of the radiation pattern is determined from the condition $L|\omega\xi|/2c < 1$, where $1/|\omega|$ is the characteristic current time. The field radiated in the vicinity

[1] We are dealing with so-called geometric volume resonances in a material with dielectric constant $\varepsilon(\omega)$. It is known that the vacuum frequency of the resonance quasi-static oscillations is determined from the condition $\varepsilon(\omega) = 0, -1, -2$ for a uniform flat layer, cylindrical column, and sphere, respectively (see, e.g., [8]). In particular, it is seen from these relations that the frequencies of the resonance oscillations of a closed plasma volume are lower than the Langmuir frequency [6, 9]. The frequency of the main (dipolar) plasma-column resonance is determined with a good accuracy by the geometric-resonance condition, even though the spatial dispersion in a finite-temperature plasma and nonuniformity of concentration profile are taken into account [10, 11].

of the maximum of the radiation pattern can be found from general expression (7) by the expansion in powers of $\xi \approx 0$:

$$\mathbf{E}(t) = -\frac{\pi a^2 L}{c^2 r}\frac{\partial}{\partial t}\mathbf{j}(t - r/c) + O(\xi^2). \quad (8)$$

It follows from this equation that, for plasma-oscillation current (3), the central frequency in the radiation spectrum along the Cherenkov cone is ω and the spectrum width is determined by the value $\nu_e/2$.

The total energy of the electromagnetic pulse is

$$W = \int_{-\infty}^{+\infty} dt \int_0^{\pi} \left\{ \frac{c}{4\pi} E^2 \right\} 2\pi r^2 \sin\vartheta d\vartheta. \quad (9)$$

By substituting the expression for the field in Eq. (9) and changing the order of integration with respect to t and ϑ, one gets, with allowance for the fact that the current is zero at $t - z/c' < 0$,

$$W = \frac{(\pi a^2)^2}{2c}\left\{ \int_0^{1-\cos\vartheta_0} w(\xi)\frac{d\xi}{\xi^2} + \int_0^{\cos\vartheta_0} w(\xi)\frac{d\xi}{\xi^2} \right\}, \quad (10)$$

where

$$w(\xi) = \int_{-L\xi/2c}^{L\xi/2c} [j(t + L\xi/2c)]^2 dt + \int_{L\xi/2c}^{\infty} [j(t + L\xi/2c) - j(t - L\xi/2c)]^2 dt. \quad (11)$$

Since the argument $t - z/c'$ of current in the latter expression can only be positive, the corresponding integration is trivial. For the plasma-oscillation current given by Eq. (3), one obtains

$$w(\xi) = j_0^2\omega^2 \exp(-\nu_e L\xi/2c)\{\cos(\omega L\xi/c) + \nu_e \sin(\omega L\xi/c)/2\omega - \exp(-\nu_e L\xi/2c)\}. \quad (12)$$

It is shown below that $\nu_e L/c \gg 1$ in the most interesting and physically realizable case. This implies that the radiation pattern is narrow and directed along the Cherenkov cone $\vartheta = \vartheta_0$. Under these conditions, the main contribution to the integral in Eq. (10) comes from ξ values close to zero, so that the upper integration limits can be set to infinity, whereupon the energy can be calculated to give the simple expression

$$W \approx \frac{(\pi a^2)^2}{c}\int_0^{\infty} w(\xi)\frac{d\xi}{\xi^2} = \frac{(\pi a^2)^2 j_0^2 L\omega}{c^2\nu_e}\arctan\frac{2\omega}{\nu_e}. \quad (13)$$

This expression is valid for any ratio between ω_p and ν_e. In the most interesting case $\omega_p \gg \nu_e$, one has

$$W \approx \frac{\pi a^4 L E_0^2 \omega_p^3}{32 c^2 \nu_e}. \quad (14)$$

A similar result can be obtained for a more general time dependence of current, provided that the Cherenkov radiation pattern is known. Indeed, the field radiated in the vicinity of the maximum of the radiation pattern is given by Eq. (8). By substituting this expression into the expression for the total radiated energy (9) and integrating with respect to the propagation angles $|\xi| < 2c/|L\omega|$, where Eq. (8) applies, one obtains

$$W \approx \frac{2(\pi a^2)^2 L}{c^2|\omega|}\int_{-\infty}^{+\infty}\left(\frac{\partial j}{\partial t}\right)^2 dt. \quad (15)$$

The expression obtained after inserting expression (3) for plasma oscillations into this formula coincides, except for a numerical factor, with Eqs. (13) and (14).

4. We now make some estimates for the discharge at atmospheric pressure. Let the plasma concentration correspond to the initial gas pressure ($N = 3 \times 10^{19}$ cm^{-3}) and the electron temperature correspond to the ionization energy ($T_e \sim 15$ eV). Then, the plasma frequency and the collisional frequency are, respectively, $\omega_p \approx 3 \times 10^{14}$ s^{-1} and $\nu_e \approx 1.5 \times 10^{13}$ s^{-1}. Therefore, the inequality $\omega_p \gg \nu_e$ is fulfilled at the normal pressure. One can then assume that Eq. (3) describes the slowly damped current oscillations with frequency $\omega \approx \omega_p/\sqrt{2}$ and initial amplitude $j_0 \approx \omega_p E_0/4\pi$. Accordingly, the central frequency of an electromagnetic pulse radiated by this current is close to $\omega/2\pi \sim 30$ THz, and the pulse duration is determined by the plasma oscillation decay time $2/\nu_e \sim 100$ fs. Note that the plasma frequency increases with pressure slower than the collisional frequency ($\omega_p/\nu_e \propto 1/\sqrt{N}$), so that both frequencies become equal to each other at a pressure on the order of 400 atm ($\omega_p \approx \nu_e \approx 6 \times 10^{15}$ s^{-1}). The corresponding radiation frequency falls into the optical range, which, however, is of little interest. Thus, the inequality $\omega_p > \nu_e$ is always fulfilled for gaseous media.

To estimate the tunnel photoionization frequency, one can use the well-known formula for the average ionization frequency of a hydrogen atom in a linearly polarized field with amplitude E_l [13]:

$$\nu_i = 4\Omega_a\sqrt{3E_a/\pi E_l}\exp(-2E_a/3E_l), \quad (16)$$

where $E_a \approx 5.14 \times 10^9$ V/cm and $\Omega_a \approx 4.16 \times 10^{16}$ s^{-1} are the "atomic" units for field and frequency, respectively. One then finds that $\nu_i > 2 \times 10^{14}$ s^{-1} for the laser intensity higher than 2×10^{14} W/cm^2, and the ionization frequency exponentially increases with intensity.

At present, the intensity on the order of 2×10^{14} W/cm^2 is quite attainable for the optical radiation in the labo-

ratory conditions, e.g., for powerful lasers with a pulse duration on the order of hundreds of femtoseconds. In particular, such an intensity was attained at the Institute of Applied Physics, Russian Academy of Sciences, on the subterawatt laser facility based on Ti:Sa crystals [14] in the experiments with optical breakdown in dense gases in the vicinity of axicon caustic [15]. With an eye to the possible demonstration experiment with the terahertz generation on this facility, we take the size of the plasma discharge region to be $L = 1$ cm and $a = 2 \times 10^{-4}$ cm [15]. Considering that the maximal strength of an external electric field is limited by the breakdown value (≈30 kV/cm at atmospheric pressure), one finds that the total energy of an electromagnetic terahertz pulse does not exceed 0.1 nJ. This energy is appreciably higher than the detection threshold of modern terahertz radiation detectors. For this reason, one can believe that the terahertz pulse can be detected experimentally if, as shown in the figure, the main portion of a pulse radiated into the Cherenkov cone is collected on a detecting element by a cylindrical focusing mirror. Note that the maximal electric field strength in the pulse at the distance $r = L$ is equal, in order of magnitude, to the strength of the applied static field ($E/E_0 \approx (a\omega_p/2c)^2 \sim 1$).

The efficiency of the suggested terahertz generation method increases with increasing concentration of the buffer gas. For example, considering that the maximal (breakdown) value of external field increases linearly with the buffer-gas pressure, one finds that the total energy of the electromagnetic pulse increases as $W \propto N^{5/2}$ and the field increases as $E \propto N^2$. The central frequency of the terahertz pulse increases with concentration as $\omega \propto N^{1/2}$. As was pointed out above, the pulse frequency is rather high (on the order of 30 THz) even at atmospheric pressure; an increase in the generation efficiency through the buildup of gas pressure will result in an even larger shift of the pulse central frequency to the visible region.

We note in conclusion that the plasma oscillations longitudinal with respect to the discharge propagation axis (so-called wake wave) can also be excited at the leading edge of the ionization pulse. The amplitude of these oscillations depends on the optical pulse envelope in a rather intricate manner; the calculation of the amplitude of these oscillations is beyond the scope of this work. We only note that the terahertz radiation produced by the longitudinal plasma-oscillation wave is also concentrated in the vicinity of Cherenkov cone and that the characteristic frequency of this radiation is higher by approximately a factor of $\sqrt{2}$ than the radiation frequency considered above.

REFERENCES

1. X.-C. Zhang, in *Ultra Fast Phenomena*, Ed. by K. Shum, Y. J. Ding, and X.-C. Zhang (Gordon and Breach, New York, 1994), CCAST-WL Series 38, pp. 89–115.
2. X.-C. Zhang and Y. Jin, in *Perspectives in Optoelectronics*, Ed. by S. S. Jha (World Sci., Singapore, 1995), pp. 81–138.
3. Zhiping Jiang and X.-C. Zhang, *Free-Space Electro-Optic Technologies, THz Sensing and Imaging Technology* (Springer, New York, 2001).
4. Qin Chen and X.-C. Zhang, in *Ultrafast Lasers: Technology and Applications*, Ed. by M. E. Fermann, A. Galvanauskas, and G. Sucha (Marcel Dekker, New York, 2001).
5. V. V. Korobkin, L. Ya. Polonsky, V. P. Popovin, and L. N. Pyatnitsky, Kvantovaya Élektron. (Moscow) **13**, 265 (1986).
6. L. Tonks, Phys. Rev. **37**, 1458 (1931); Phys. Rev. **38**, 1219 (1931).
7. A. Dattner, Ericsson Technics **2**, 309 (1957); Ericsson Technics **8**, 1 (1963); Phys. Rev. Lett. **10**, 205 (1963).
8. N. A. Krall and A. W. Trivelpiece, *Principles of Plasma Physics* (Academic, New York, 1973; Mir, Moscow, 1975).
9. A. W. Trivelpiece and R. W. Gould, J. Appl. Phys. **30**, 1784 (1959).
10. P. E. Vandenplas and R. W. Gould, Plasma Phys. **6**, 449 (1964).
11. J. V. Parker, J. C. Nickel, and R. W. Gould, Phys. Rev. Lett. **11**, 183 (1963); Phys. Fluids **7**, 1489 (1964).
12. L. D. Landau and E. M. Lifshitz, *The Classical Theory of Fields*, 6th ed. (Nauka, Moscow, 1973; Pergamon Press, Oxford, 1975), Vol. 2.
13. N. V. Vvedenskiĭ and V. B. Gil'denburg, Pis'ma Zh. Éksp. Teor. Fiz. **76**, 440 (2002) [JETP Lett. **76**, 380 (2002)].
14. A. A. Babin, A. M. Kiselev, K. I. Pravdenko, *et al.*, Usp. Fiz. Nauk **169**, 81 (1999) [Phys. Usp. **42**, 74 (1999)].
15. S. Bodrov and D. Kulagin, *Technical Digest of IQEC/LAT-YS 2002* (Moscow, 2002), p. 47.

Translated by V. Sakun

JETP Letters, Vol. 79, No. 8, 2004, pp. 365–367. Translated from Pis'ma v Zhurnal Éksperimental'noĭ i Teoreticheskoĭ Fiziki, Vol. 79, No. 8, 2004, pp. 448–451.

Terahertz Electroluminescence under Conditions of Shallow Acceptor Breakdown in Germanium

A. V. Andrianov*, A. O. Zakhar'in, I. N. Yassievich, and N. N. Zinov'ev

Ioffe Physicotechnical Institute, Russian Academy of Sciences, Politekhnicheskaya ul. 26, St. Petersburg, 194021 Russia

**e-mail: alex.andrianov@mail.ioffe.ru*

Received March 4, 2004

The spectrum of spontaneous terahertz electroluminescence was obtained near the breakdown threshold of a shallow acceptor (Ga) in germanium. The emission spectra were recorded by the Fourier spectroscopy method at a temperature of ~5.5–5.6 K. The emission spectrum exhibits narrow lines with maxima at ~1.99 THz (8.2 meV) and ~2.36 THz (9.7 meV), corresponding to the optical transitions of nonequilibrium holes from the excited impurity states to the ground state of impurity center. A broad line with a maximum at ~3.15 THz (13 meV) corresponding to the hole transitions from the valence band to the impurity ground state is also seen in the spectrum. The contribution of the hole transitions from the states of the valence band increases upon an increase in the electric-field strength. Simultaneously, the optical transitions of nonequilibrium holes between the subbands of the valence band appear in the emission spectrum. The integral terahertz-emission power is ~17 nW per 1 W of the input power. © *2004 MAIK "Nauka/Interperiodica".*

PACS numbers: 78.60.Fi; 07.57.Hm

At present, the terahertz (THz) range of electromagnetic spectrum (also referred to as the far-infrared region) is being intensively studied. Interest in terahertz radiation is due to the prospects of its use in many highly important fields of science and technology, such as condensed state physics, medicine, biology, and communication and remote control techniques. The demonstration of a unipolar semiconductor THz laser operating on the intrasubband optical electronic transitions in the quantum cascade structures [1] may give impetus to the fabrication of solid-state current-excited monochromatic THz sources. Optically pumped semiconductor lasers, in which the THz oscillation is due to the photoionization of impurity centers followed by the photocarrier transitions from the allowed band to the impurity states, have also been devised in recent years [2]. The authors of [3] report the observation of an intense spontaneous THz emission arising upon the impurity electrical breakdown in a Si(B)-based structure. In germanium, fields corresponding to the collisional ionization of shallow acceptors are appreciably lower than in silicon and are as low as a few V/cm [4–7]. The THz emission induced by the collisional ionization of shallow impurities (As, Sb) was first observed in germanium in [4]. The spontaneous emission spectra under the conditions of electrical breakdown of shallow impurities (As, Sb, P) were recorded in [5, 6]. Although the integral THz emission induced by the collisional ionization of shallow acceptors in germanium was observed in many works (see, e.g., [7, 8] and references therein), the study of the spontaneous THz-emission spectra under the breakdown conditions has not been carried out so far. However, the transitions between the states of a shallow acceptor (Ga) under the conditions of electrical breakdown in the impurity germanium are precisely those which were suggested for the implementation of the resonance-state lasing mechanism [9]. That is why the experimental spectroscopic study of the radiative transitions induced by trapping the nonequilibrium holes on the acceptor levels in germanium is a highly topical problem. In this work, the spontaneous THz-emission spectrum under the conditions of electrical breakdown of a shallow acceptor (Ga) in Ge was obtained near the impurity breakdown threshold.

Samples were prepared from *p*-Ge(Ga) with a resistivity of 10 Ω cm ($N_A - N_D = 4 \times 10^{14}$ cm^{-3}) and shaped like rectangular platelets 15×6 mm in size and 1.5 mm in thickness. The ohmic contacts were made by fusing indium with gallium into lateral faces of an area of 1.5×15 mm. The samples were mounted on the copper cold finger of a helium optical cryostat. An OST 38 0183-75 vacuum lubricant was used for mounting, because it possesses a high thermal conductivity and provides good electrical insulation of the sample from the cold finger of the cryostat. The sample under study was enclosed with copper helium and nitrogen screens with windows made from black polyethylene and germanium, respectively. The warm cryostat window was made from a TPX material. The temperature at the cold finger was monitored by a calibrated germanium resistance thermometer placed in the immediate vicinity of the sample. A bias on the sample was applied in the form of pulse "bundles." Pulse duration in a bundle was 10 μs for a frequency of 50 kHz. The bundle duration and frequency were 6.2 ms and 80 Hz, respectively.

0021-3640/04/7908-0365$26.00 © 2004 MAIK "Nauka/Interperiodica"

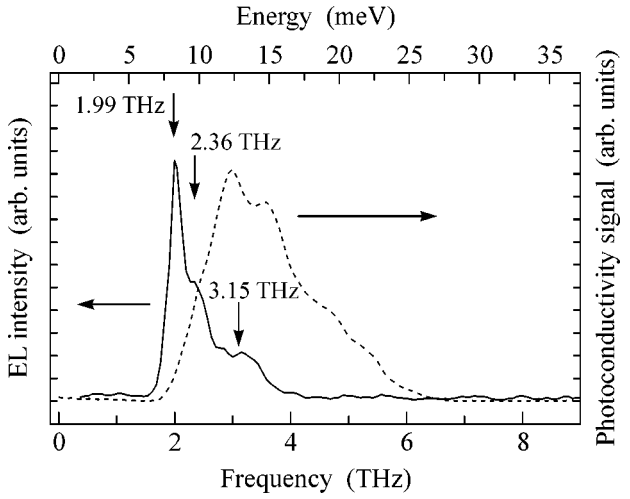

Fig. 1. The solid line is the THz-emission spectrum at 4.5 V and $T = 5.5$ K, and the dashed line is the photoconductivity spectrum. Signals are not normalized to the spectral sensitivity of the measuring system.

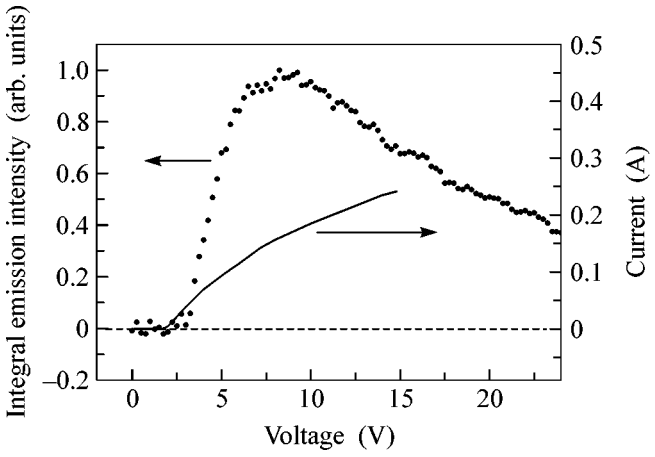

Fig. 2. The integral THz-emission intensity as a function of the bias on the *p*-Ge(Ga) sample with $N_A - N_D = 4 \times 10^{14}$ cm^{-3} (points). Voltage dependence of the current through the sample (solid curve). The dashed line is the zero-signal level. The temperature in these experiments was 5.5–5.7 K.

A liquid-helium-cooled silicon bolometer (QMC Instruments) equipped with a passband optical filter to provide operation in the spectral range 2–400 cm^{-1} (0.06–120 THz) served as the detector of the THz emission. The detector signal was measured using an SR-530 lock-in amplifier. The emission spectra were recorded by a pump-out Fourier transform spectrometer (the description of the experimental setup is given in [10, 11]). The low-temperature photoconductivity spectra were also measured for the Ge(Ga) samples. In this case, an emitter of the "black body" type with a tungsten filament heated by electric current was used.

The THz-emission spectrum measured for a bias of 4.5 V on the contacts (the corresponding field strength is ~7.5 V/cm) and a temperature of 5.5 K at the cold finger is presented in Fig. 1. The photoconductivity signal measured for the same Ge(Ga) sample is also shown in this figure. The spectra were recorded with a resolution of ~0.3 THz (~1.2 meV). The typical dependence of the current on the voltage applied to the *p*-Ge sample and the dependence of the integral THz-emission intensity on the voltage amplitude are shown in Fig. 2.

One can see (Fig. 2) a drastic increase in the current through the sample upon the occurrence of the impurity electrical breakdown at a voltage V of ~2 V between the contacts, which corresponds to a breakdown field of ~3.3 V/cm. This value of the impurity breakdown field in Ge(Ga) correlates with the data of other authors (see, e.g., [7] and references therein). One can also see from Fig. 2 that the THz emission arises upon reaching the impurity breakdown. The emission intensity increases drastically at $V > 2$ V, reaches maximum at $V \sim 8.3$ V (field strength ~13.8 V/cm), and then decreases with increasing voltage. A maximum in the curve of integral intensity as a function of voltage was observed in Ge(Ga) at fields ~15–20 V/cm [7] and assigned to the intraband radiative transitions of nonequilibrium holes. In [7], a slight decrease in the emission intensity with increasing field strength in the range from 20 to 100 V/cm was assigned to the streaming of the hole distribution function in a strong electric field. A drop in the THz-emission intensity observed in our experiment at $V > 8.3$ V is more pronounced than in [7] and can be caused, in addition to the aforementioned mechanism, by the influence of lattice heating at voltages 10–25 V.

The emission spectrum near the impurity breakdown threshold (Fig. 1) shows a narrow line with a maximum at 1.99 THz (8.25 meV), whose position is close to the impurity photoconductivity signal threshold. The narrow intense emission line at 1.99 THz can be assigned to the optical transition from the first excited to the ground state of Ga impurity in germanium (2*p*–1*s* transition), in good agreement with a value of 10.8 meV known from literature for the impurity binding energy [12]. The high-frequency asymmetry of the main line can be caused by the contribution from a narrow line with a maximum at ~2.36 THz (9.7 meV) and a broad line with a maximum at ~3.15 THz (13 meV). The line at 2.36 THz corresponds to the transition from one of the impurity excited states (e.g., $n = 3$) to the ground state. The emission at 3.15 THz is most probably due to the transitions of hot holes to the impurity ground state, while the characteristic energy of the holes involved in this transition should be ~2.2 meV (effective temperature ~26 K). The Monte Carlo calculations [13] of the nonequilibrium distribution function for the holes generated into the valence band through the collisional ionization of shallow acceptors in electric fields of ~7 V/cm yield a value close to the indicated hole effective temperature in germanium. Future measurements of THz emission with a

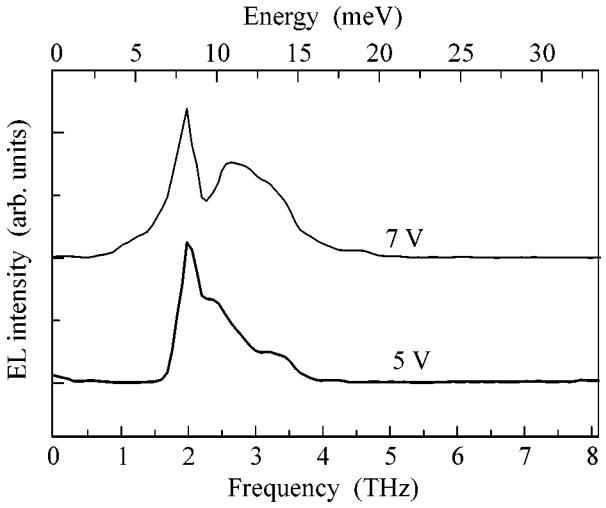

Fig. 3. The THz-emission spectra at 5 and 7 V. The spectra are normalized to the signal maximum and vertically shifted for clarity. The signals are not normalized to the spectral sensitivity of the measuring system. It should be noted that the dip observed at ~2.35 THz is most probably due to the absorption in the optical filter of the QMS bolometer. To eliminate this distortion in the spectrum, further measurements are required.

higher spectral resolution will allow a more detailed study of the spectral structure.

The THz-emission spectra measured at voltages of 5 and 7 V are shown in Fig. 3. In both cases, the cold finger temperature did not exceed 5.6 K and was lower for 5 V. One can see that the emission spectrum changes substantially with a rise in field strength. The contribution from the optical transitions of hot holes from the valence band to the impurity ground state increases. The pronounced low-frequency wing appearing in the $2p$–$1s$ line can be due to the contribution from the intraband radiative optical transitions of nonequilibrium holes, resulting in THz emission at frequencies of ~0.75–1.65 THz (3.1–6.8 meV).

The estimates of the THz radiation power with regard to the corrections for receiving radiation and delivering it to the detector give a value of ~17 nW for a p-Ge sample ($N_A - N_D = 4 \times 10^{14}$ cm^{-3}) of size $1.5 \times 1.5 \times 6$ mm^3 and an input electrical power of 1 W at $T = 5.6$ K. A high intensity of THz emission arising in p-Ge(Ga) upon the radiative hole capture on the impurity level may become an important factor in the design of relatively simple and inexpensive electrically pumped THz emitters in the ~2 THz range.

We note in conclusion that the spectra of spontaneous THz electroluminescence near the breakdown threshold of a shallow acceptor (Ga) in germanium have been obtained in this work. The narrow lines corresponding to the hole transitions between the excited states and the ground state of an impurity center are clearly seen in the spectra. A feature caused by the hole transitions inside the valence band and by the transitions from the valence band states to the impurity ground state has also been identified in the emission spectra. A high quantum yield of radiative transitions can become an important factor in designing electrically pumped THz emitters in the range ~2 THz.

This work was supported by the Russian Foundation for Basic Research (project no. 03-02-17512), ISTC (grant no. 2206p), CRDF (grant no. RP-2-2552-MO-03), and (in part) the program of the Presidium of the Russian Academy of Sciences “Low-Dimensional and Quantum Structures.”

REFERENCES

1. R. Köhler, A. Tredicucci, F. Beltram, *et al.*, Nature **417**, 156 (2002).
2. S. G. Pavlov, R. Kh. Zhukavin, E. E. Orlova, *et al.*, Phys. Rev. Lett. **84**, 5220 (2000).
3. T. N. Adam, R. T. Troeger, S. K. Ray, *et al.*, Appl. Phys. Lett. **83**, 1713 (2003).
4. S. H. Koenig and R. D. Brown, Phys. Rev. Lett. **4**, 170 (1960).
5. S. N. Solomon and H. Y. Fan, Phys. Rev. B **1**, 662 (1970).
6. S. R. Thomas and H. Y. Fan, Phys. Rev. B **9**, 4295 (1974).
7. L. V. Berman, L. I. Gavrilenko, Z. F. Krasil’nik, *et al.*, Fiz. Tekh. Poluprovodn. (Leningrad) **19**, 369 (1985) [Sov. Phys. Semicond. **19**, 231 (1985)].
8. Yu. L. Ivanov, in *Problems in the Physics of Semiconductors: Proceedings of XI Winter School on the Physics of Semiconductors* (Fiz.–Tekh. Inst., Leningrad, 1984), p. 160.
9. Yu. P. Gousev, I. V. Altukhov, V. P. Sinis, *et al.*, Appl. Phys. Lett. **75**, 757 (1999).
10. N. N. Zinov’ev, A. V. Andrianov, V. N. Nekrasov, *et al.*, Pis’ma Zh. Éksp. Teor. Fiz. **74**, 105 (2001) [JETP Lett. **74**, 100 (2001)].
11. N. N. Zinov’ev, A. V. Andrianov, V. N. Nekrasov, *et al.*, Fiz. Tekh. Poluprovodn. (St. Petersburg) **36**, 234 (2002) [Semiconductors **36**, 226 (2002)].
12. R. Newman and W. W. Tyler, in *Solid State Physics*, Ed. by F. Seitz and D. Turnbull (Academic, New York, 1959), Vol. 8, p. 50.
13. W. Quade, G. Hupper, and E. Schöll, Phys. Rev. B **49**, 13408 (1994).

Translated by V. Sakun

JETP Letters, Vol. 79, No. 8, 2004, pp. 368–371. Translated from Pis'ma v Zhurnal Éksperimental'noĭ i Teoreticheskoĭ Fiziki, Vol. 79, No. 8, 2004, pp. 452–456.

Dynamic Interaction of Plasma Flow with the Hot Boundary Layer of a Geomagnetic Trap

S. P. Savin[1], L. M. Zelenyi[1], E. Amata[2], J. Buechner[3], J. Blecki[4], S. I. Klimov[1], B. Nikutowski[3], J. L. Rauch[5], S. A. Romanov[1], A. A. Skalsky[1], V. N. Smirnov[1], P. Song[6], and K. Stasiewicz[4]

[1] *Space Research Institute, Russian Academy of Sciences, Moscow, 117997 Russia*
[2] *Interplanetary Space Physics Institute, CNR, 00133 Rome, Italy*
[3] *Max-Planck Institut Aeronomie, 37191 Katlenburg-Lindau, Germany*
[4] *Space Research Center, 00716 Warsaw, Poland*
[5] *Lab Physics Chemistry Environment, 30037 Orleans, France*
[6] *University of Massachusetts, Lowell, MA 01854, USA*

Received March 2, 2004

The study of the interaction between collisionless plasma flow and stagnant plasma revealed the presence of an outer boundary layer at the border of a geomagnetic trap, where the super-Alfvén subsonic laminar flow changes over to the dynamic regime characterized by the formation of accelerated magnetosonic jets and decelerated Alfvén flows with characteristic relaxation times of 10–20 min. The nonlinear interaction of fluctuations in the initial flow with the waves reflected from an obstacle explains the observed flow chaotization. The Cherenkov resonance of the magnetosonic jet with the fluctuation beats between the boundary layer and the incoming flow is the possible mechanism of its formation. In the flow reference system, the incoming particles are accelerated by the electric fields at the border of boundary layer that arise self-consistently as a result of the preceding wave–particle interactions; the inertial drift of the incoming ions in a transverse electric field increasing toward the border explains quantitatively the observed ion acceleration. The magnetosonic jets may carry away downstream up to a half of the unperturbed flow momentum, and their dynamic pressure is an order of magnitude higher than the magnetic pressure at the obstacle border. The appearance of nonequilibrium jets and the boundary-layer fluctuations are synchronized by the magnetosonic oscillations of the incoming flow at frequencies of 1–2 mHz. © *2004 MAIK "Nauka/Interperiodica".*

PACS numbers: 52.40.Hf; 52.30.-q; 52.40.-w

This work is devoted to the experimental study of the dynamic interaction of plasma flow with a local obstacle in which the transverse pressure of hot plasma dominates: $\beta_i = nT_i/W_b > 2$ ($W_b = B^2/8\pi$ is the magnetic pressure, n is the ion density, and T_i is temperature; all energy quantities are in eV/cm^3 (Fig. 1)). This occurs over the magnetic poles of traps in the regions, where the absolute value of magnetic field is minimal and which are filled with external (originally) plasma (Fig. 1b). This work is the continuation of our work [1], where the opposite limiting case of plasma deceleration and chaotization by a "rigid" magnetic barrier was considered. The main distinction is that the flow regime considered in this work is inhomogeneous and nonstationary, in which the flow kinetic energy does not fully transform into nonlinear wave cascades in the stagnation region ahead of the obstacle [1], but first is "released" downstream in the accelerated magnetosonic jets. The plasma–plasma interaction proceeds through large-amplitude waves. It is anticipated that the dynamic flow regime considered in this work will throw light on the mass- and energy-transfer processes at the borders of astrophysical objects and laboratory traps and allow the study of plasma–plasma interaction remotely using secondary radiations in accelerated inhomogeneous jets.

We illustrate the interaction between the incident and stagnant plasmas by the example of the Interball-1 satellite data on June 19, 1998 (Fig. 1). In Fig. 1a, the spectrogram of the intensity of ion kinetic-energy fluctuations is given for $W_{\text{kin}} = 0.5nM_iV_i^2$ (M_i and V_i are the proton mass and velocity, respectively) and the main waves are shown (see also Fig. 2 and [2]). The transition from the unperturbed equilibrium flow (from the left in Fig. 1b) to the boundary layer near the trap border (magnetopuase (MP)) is shown in Fig. 1b. The satellite was brought into the trap near the magnetic-field bifurcation over the trap magnetic pole (the field had a nonzero upward projection at the top of the border and a nonzero downward projection at the bottom), where the magnetic density is low and an inner boundary layer (cusp) filled with a heated solar plasma ("plasma ball" [2]) is formed. The flow, on average, is subsonic, and the ion pressure nT_i dominates; the domains with $W_{\text{kin}} > W_b$ (Fig. 1c) correspond to the super-Alfvén flow [2]. In

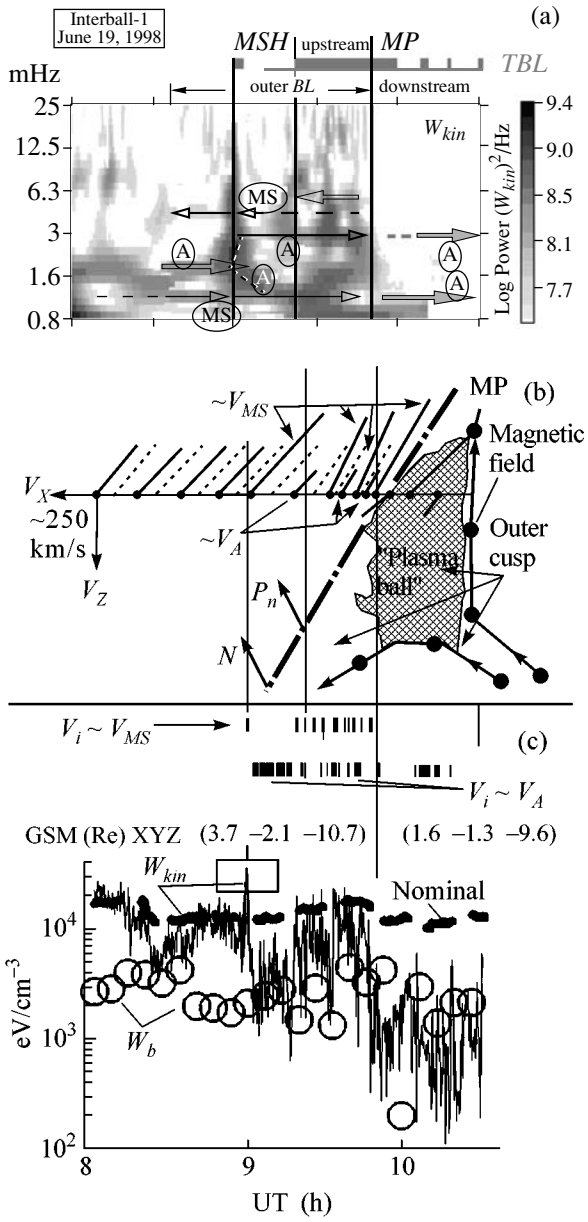

Fig. 1. (a) Morlet wavelet transformation [1, 2] of the ion kinetic-energy density $W_{\rm kin}$ on June 19, 1998. Arrows indicate the propagation directions of the Alfvén (A) and magnetosonic (MS) waves. (b) Vectors of plasma velocity along the Interball-1 satellite orbit in the *XZ* plane of the geocentric solar ecliptic (GSE) coordinate system (dashes: nominal values [2]); *N* is the normal to the magnetopause (MP) ~ (0.7, 0.07, –0.71) [2]; the MP is denoted by a heavy line with discontinuities; and the magnetic field **B** is shown by the arrowed curves with circles. (c) Energy densities $W_{\rm kin}$ (nominal value is shown by bold dashes; see [2]) and (circles) W_b in eV/cm^3. The first MS jet is indicated by the rectangle, and the instants of time at which the ion velocity (V_i) was close to the magnetosonic (V_{MS}) and Alfvén (V_A) velocities are shown at the top of Fig. 1c.

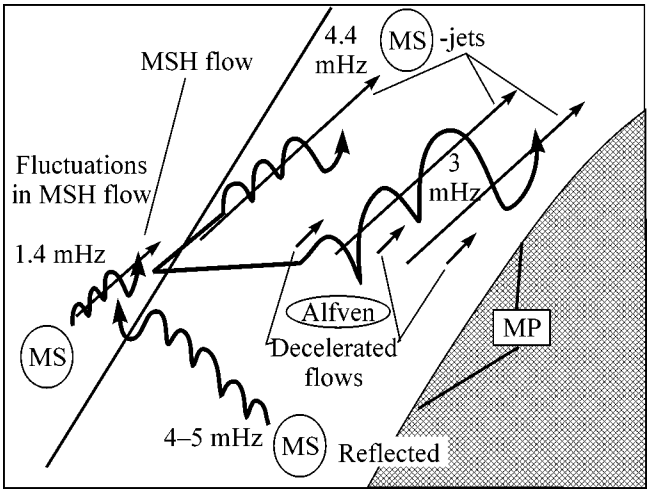

Fig. 2. Scheme of interaction between the magnetosonic waves in magnetosheath (MSH; 1.4 mHz; see Fig. 1a) and the reflected MS waves (4–5 mHz), and the decay into the accelerated MS jet (4.4 mHz) and decelerated Alfvén waves (Alfvén; 3 mHz).

contrast to [1], W_b rapidly drops immediately under the MP ($\beta_i \sim 15$). At 09:00 UT, the measured $W_{\rm kin}$ exceeds the nominal value by a factor of 2.5, which corresponds to the appearance of the first accelerated plasma jet with a velocity close to $V_{MS} \sim (2T_i/M_i)^{1/2}$, i.e., a magnetosonic (MS) velocity at high β_i (MS jet at 09:00 UT). Thereafter, a decelerated Alfvén flow (A) arises, as follows from the fact that $W_{\rm kin} \sim W_b$, i.e., $V_i \sim V_A = B/(nM_i)^{1/2}$, where V_A is the Alfvén velocity. The relaxation time of the slow jet is on the order of 10–20 min. The MS and A domains are marked off by black rectangles at the top of Fig. 1c. Since the dynamic pressure of the first MS jet is as high as its value in solar wind and, hence, far exceeds the magnetic pressure even deep inside the obstacle (Fig. 1c), such jets, when flowing around complex magnetic configurations, can distort the boundary and even penetrate it (cf. "impulsive penetration" in [3]) at large angles of incidence relative to the average flow (as in [1]). Hence, the phenomenon discussed here should have an appreciable effect on the flow process and on the local shape of the obstacle.

At 09:00 UT, the projection of the Poynting's vector onto the normal to MP (**N** in Fig. 1b; see [2]) is $P_n < 0$, indicating that the corresponding perturbation approaches the MP (i.e., the reconnection of magnetic fields at the MP cannot be its source). The average flow $n|\mathbf{V}_i|$ at 08:55–09:55 UT decreases by more than 40% with respect to its nominal value (cf. $W_{\rm kin}$ in Fig. 1c), which, at first glance, points to the fact that the momentum conservation law is violated (after time averaging). However, the MS jet formed in the unperturbed flow moves in the **N** direction with the velocity of the surrounding flow, while the rest of the boundary layer moves together with the MP. Inasmuch as the velocity of the unperturbed flow is, approximately, an order of magnitude higher than the MP velocity [2, 3], the

momentum conservation law is obeyed after averaging over the distance along **N**.

The reliable detection of the waves reflected from the obstacle with the use of the Poynting's vector is one of our main experimental results. After 09:00 UT, reflected waves with $P_n > 0$ are repeatedly seen [2]. From 08:35 UT, intense bursts with $P_n < 0$ (downstream) appear, which are unrelated to the perturbations in the external flow (cf. the nominal value of W_{kin} in Fig. 1c and [2]); i.e., they correspond to the downstream momentum release.

At low frequencies, only the MS wave can propagate counter to the super-Alfvén flow (the Alfvén Mach number is >2) [3, 4]. By comparing the ion-density N_i and velocity V_{ix} spectrograms with allowance for the Poynting's vector [2], we determined the wave types in the essentially nonlinear situation: the reflected MS waves with a weak maximum at 4–6 mHz (marked "MS" and "Reflected" and by the leftward arrow in Figs. 1a and 2; for them, $P_n > 0$) interact at 1.4 mHz with the MS wave in the incoming flow. This results in the oscillation amplification and gives rise to an A wave at 1.7–2.2 mHz. The process ends at 09:00 UT in the MS jet generation, shown in Fig. 1a as a decay of the initial oscillations into the MS-jet and Alfvén waves (3 mHz, Alfvén). At 09:15–09:45 UT, the reflected waves at 5–6 mHz initiate multiple MS/A decays.

Three periods $T_1 \sim 13$ min corresponding to a frequency of 1.4 mHz cover the entire outer boundary layer. This frequency modulates the spectral maxima at 3–10 mHz. This fact conforms with a "thick" turbulent boundary layer (TBL) [1] (rather than with a thin shock front), where equilibrium is attained within several periods (T_1) of the main oscillation that synchronizes the phases of all the interactions, from the unperturbed flow to the TBL and plasma ball. The phase synchronization is evident from the bicoherent character of V_{ix}, which sets off the processes with frequencies $f_s = f_l + f_k$ (see [1, 2]): the bicoherence is appreciable only if the phases of the three processes are synchronized. We assign the bicoherence maximum at 1.4 mHz + 3 mHz = $f_l + f_k = f_s = 4.4$ mHz with an amplitude of ~75% to the decay of the stationary flow into the nonstationary MS/A flows. The phase synchronization at these frequencies provides the interplay between the processes prior to the jet formation in the boundary layer. The most intriguing experimental fact is that the initial flow decays precisely into the MS/A flows. It is likely that this is one of the most prominent examples of three-wave decay in plasma; each of the secondary waves consists of flows propagating with the corresponding characteristic velocity. So far, the presence of accelerated plasma in the boundary layer was regarded as evidence that the energy accumulated in a magnetic field compressed by an external flow transforms during the process of reconnection of the flow and trap magnetic fields in a hypothetically small region, where the plasma freezing-in breaks down due to the efficient conduction [3]. In the case of the initially antiparallel magnetic fields, the acceleration to the Alfvén velocity is due to the magnetic tension. However, the Alfvén Mach number in the MS jet is higher than 3, which, with allowance for the fact that the mean $\beta_i > 2$, excludes the local magnetic-field reconnection as a cause of jet acceleration. To reveal the acceleration mechanism for the jets near the magnetopause, it is convenient to compare their dynamic pressure with the magnetic pressure inside the obstacle, because the upper limit for W_{kin} upon the reconnection is $0.5nM_iV_A^2 \sim W_b$; i.e., it depends only on $|\mathbf{B}|$. In the case of $W_{\text{kin}} \gg W_b$ (as in Fig. 1c), an alternative plasma-acceleration mechanism based on the direct flow-energy transformation without the intermediate energy accumulation in the distorted magnetic field is expected to be operative. This mechanism (the structurization of nonlinear oscillations) is the opposite of the flow thermalization in the shock wave, as regards the increase in the ordered MS-jet velocity. For plasma, it turns out to be energetically more profitable to "release" downstream the excess of its momentum through the acceleration of its small portion and pass to the decelerated Alfvén flow closer to the obstacle border (Fig. 2). This process can be described using the formalism corresponding to the maser-type mechanism of formation of magnetosonic solitons ([5]): the system radiates a coherent magnetosonic packet (MS jet) and turns to the stable state with the Alfvén flow. If the fast and slow flows are spatially separated, the slow flow starts to interact with the newly incoming super-Alfvén flow to relax to its nominal level or initiate oscillations in the outer boundary layer.

Thus, the study of the plasma-flow interaction with a geomagnetic trap gives evidence that the laminar flow transforms into nonstationary magnetosonic jets and decelerated Alfvén flows behind the shock wave. They are involved in a unified synchronized process of interaction in the outer boundary layer ("outer BL" in Fig. 1a), whose thickness is estimated at 1–2 Earth radii R_E for a distance of $\sim 10R_E$ between the MP and the Earth. The characteristic (synchronizing) frequency of ~1.4 mHz can be assigned to the resonance plasma oscillations between the dayside magnetopause and the shock wave (Yu.I. Gal'perin, private communication, 2001).

The frequencies f_l and f_k (1.4 and 3 mHz in Fig. 2) relate to the time domain in the MP system, because the corresponding maxima are seen at practically the same frequencies over a wide range of flow velocities (and, hence, Doppler shifts; see Fig. 1 and [2]).

Neglecting the MS-jet oscillation frequency compared to the Doppler shift and using the frequency summation rule $f_l + f_k = f_s$ in bi-spectra, we obtain the condition for the Cherenkov resonance of the jet with the fluctuation beats between the incoming flow and the

boundary layer in the case of interacting media moving relative to each other (cf. [4]):

$$f_l + f_k = \mathbf{kV}/2\pi, \quad (1)$$

where **V** is the mean velocity of the unperturbed plasma in the MP system, where the interaction takes place, and **k** is the wave vector. The characteristic MS-jet size along the flow can be estimated as $L = |\mathbf{V}|/(f_l + f_k) \sim 5R_E$, in compliance with the above assumption that the MS jet and the corresponding A flow are spatially separated if the characteristic transverse size of the streamlining zone is $\sim 20R_E$.

We now consider quantitatively the plasma acceleration in a nonuniform external transverse electric field encountered by the unperturbed flow at the border of the outer boundary layer. This interaction is similar to the Fermi acceleration induced by the boundary-layer border (inclined "wall") moving toward the $+X$ axis in the plasma reference system (MSH; Fig. 2). The magnetosonic velocity V_{MS} is the asymptotic value of mean velocity of an initially subsonic jet. For the mean plasma velocity **V** ~ (–170, –70, –80) km/s at 08:54–08:58 UT, we calculated the electric field in the plasma reference system; it increased to 8 mV/m in the MS-jet region. Since the time resolution (10 s) is smaller than the proton gyroperiod (2–3 s), while the lower estimate of the jet width (300 km for the projection of the boundary-layer velocity behind the jet onto the normal to MP) exceeds the proton gyroradius (~100 km), we use the inertial-drift approximation [6] with the drift velocity

$$\mathbf{V}_d^{(1)} = 1/(M\omega_H^2)d\mathbf{F}/dt = Ze/(M\omega_H^2)d\mathbf{E}/dt, \quad (2)$$

where M, ω_H, and Ze are the particle mass, cyclotron frequency, and charge, respectively, and **F** and **E** are the transverse force and electric field, respectively. The upper index (1) denotes first order in the small parameter, as compared to the zero-order drift approximation for uniform fields. Then, the energy increment is defined as [6]

$$\delta W_{\text{kin}} \sim \delta(nM(\mathbf{V}_d^{(0)})^2/2), \quad (3)$$

where the gradient-drift velocity in an electric field is $\mathbf{V}_d^{(0)} = c[\mathbf{E} \times \mathbf{B}]$ (c is the speed of light and **B** is the magnetic vector). The value $\delta W_{\text{kin}} \sim 30$ keV/cm^3 obtained from Eq. (3) for the measured parameters agrees well with the maximal density $W_{\max} \sim 35$ keV/cm^3 of the jet kinetic energy and with the mean value $W_{\text{kin}} \sim 7$ keV/cm^3 immediately ahead of the jet (Fig. 1c). Moreover, it follows from Eq. (2) that the ions and electrons drift in different directions. This explains the appearance of "intermittent" current layers with anomalously high statistic of large magnetic-field rotation angles in the turbulent boundary layer [2].

We note in conclusion that the process of streamlining nearby the plasma–plasma boundary is nonequilibrium on a time scale comparable with the characteristic observation time of Alfvén flows (10–20 min). Instead of a gradual plasma acceleration near the side walls of the obstacle, accelerated and decelerated jets are observed. The accelerated jets carry away downstream the difference in momenta of the unperturbed flow and the flow decelerated in the outer boundary layer. The dynamic pressure of the jets is so high that they can distort the local boundary of the obstacle and penetrate into it at large angles of incidence.

This work was supported by the Russian Foundation for Basic Research (project nos. 02-02-17160, 03-02-16967, 04-02-17371), the International Space Science Institution, INTAS (grant nos. 03-51-4872, 03-51-3738), and HPRN-CT-2001-00314.

REFERENCES

1. S. P. Savin, L. M. Zelenyi, S. A. Romanov, *et al.*, Pis'ma Zh. Éksp. Teor. Fiz. **74**, 620 (2001) [JETP Lett. **74**, 547 (2001)].
2. S. Savin, A. Skalsky, L. Zelenyi, *et al.*, Surv. Geophys. (2004) (in press).
3. B. Hultqvist, M. Oieroset, G. Paschmann, and R. Treumann, *Magnetospheric Plasma Sources and Losses* (Kluwer Academic, Dordrecht, 1999); D. G. Sibeck, G. Paschmann, R. Treumann, *et al.*, Space Sci. Rev. **88** (1–2), 207 (1999).
4. A. A. Galeev and R. Z. Sagdeev, in *Basic Plasma Physics*, Ed. by A. A. Galeev and R. Sudan (Énergoatomizdat, Moscow, 1983; North-Holland, Amsterdam, 1984), Vol. 1.
5. K. Stasiewicz, P. K. Shukla, G. Gustafsson, *et al.*, Phys. Rev. Lett. **90**, 085002 (2003).
6. V. E. Golant, A. P. Zhilinskiĭ, and S. A. Sakharov, *Fundamentals of Plasma Physics* (Atomizdat, Moscow, 1977; Wiley, New York, 1980).

Translated by V. Sakun

JETP Letters, Vol. 79, No. 8, 2004, pp. 372–374. Translated from Pis'ma v Zhurnal Éksperimental'noĭ i Teoreticheskoĭ Fiziki, Vol. 79, No. 8, 2004, pp. 457–459.

Droplet Cluster

A. A. Fedorets

Tyumen State University, ul. Semakova 10, Tyumen, 625003 Russia
e-mail: fedorets_alex@utmn.ru

Received January 20, 2004; in final form, March 15, 2004

A new phenomenon consisting of the formation of an ordered layer of condensate microdroplets at the water free surface was observed upon the irradiation of an open horizontal water layer (and layers of some organic fluids) by a light beam that causes local heating and evaporation of the fluid. © *2004 MAIK "Nauka/Interperiodica".*

PACS numbers: 44.25.+f; 47.55.Dz

A new phenomenon was observed in the course of studying the photoinduced thermocapillary flows [1, 2] using an MBS-10 microscope equipped with an accessory for photography and video recording. An open thin water layer on an ebonite substrate was one of the systems under study. In an effort to improve video recording conditions, a beam from an OI-9M illuminator (with a filament-lamp power of 20 W) was focused on a substrate and caused local heating and evaporation of a fluid. As a result, a steam-and-air convective flame, which showed up as a movable fog stub, arose over the illuminated region (8 × 10 mm rectangular area). The behavior of the condensate droplets that fell out from the stub to the layer proved to be highly surprising. These droplets, shaped like miniature balls, moved over the free surface and did not coalesce with the layer or with each other. Though falling to different layer areas, the droplets directed to a common center to form an ordered structure from tens and hundreds of droplets, hereafter referred to as a droplet cluster (Fig. 1). The droplet stability time in the cluster could easily be determined, because the destruction of one of the droplets entailed the "disappearance" of a large segment comprising several tens of droplets (Fig. 2). It turned out that, under fixed external conditions, the detected cluster stability period was limited by the time of continuous observation and was longer than 10 min.

To date, searching experiments have been carried out with unboiled and boiled tap water, distilled water, and a number of organic liquids (butanol, benzyl alcohol, glycerol) on ebonite, carbolite, and stained glass substrates and with various light-beam intensities, fluid-layer thicknesses, and evaporation regimes (open or closed cuvette). Despite the qualitative character of these experiments, they allowed the revelation of a number of important features of the droplet clusters and, in particular, the conditions necessary for their reproduction.

The main results which can elucidate the nature of this phenomenon can be generalized as follows.

1. *Irrespective of the substrate substance, the phenomenon was reproduced for all water, benzyl alcohol, and glycerol samples and was not observed for the butanol layers. All fluid samples, for which the droplets*

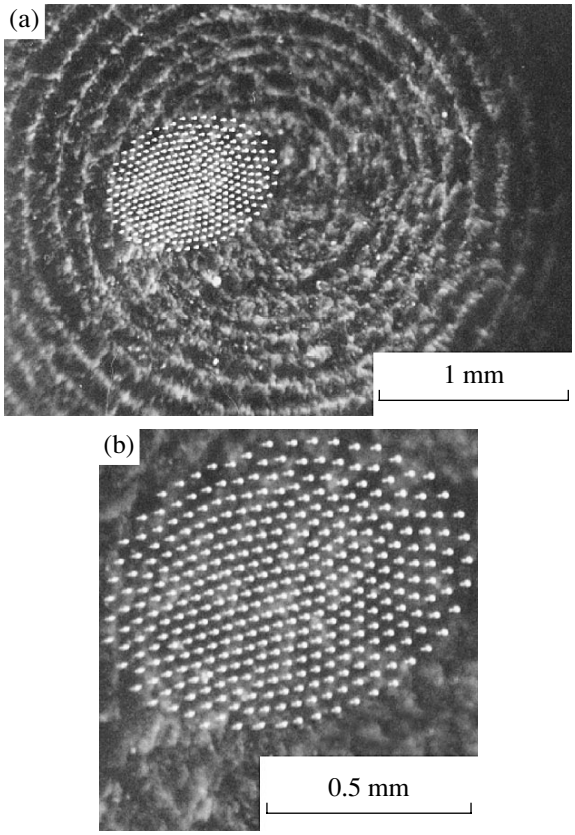

Fig. 1. (a) Typical droplet cluster. Water layer on an ebonite substrate. Circular grooves are the traces of the substrate processing on a lathe; a photograph of the object is given in the lower right corner. (b) Enlarged cluster image.

0021-3640/04/7908-0372$26.00 © 2004 MAIK "Nauka/Interperiodica"

were stabilized, were contaminated with surface-active substances (SASs).

2. *The phenomenon depends on the thermal action of the light.* (a) It appears only if either the substrate or fluid strongly absorbs the light to heat and evaporate the layer; (b) after a dark pause, the droplets do not lose stability as long as the pause duration is shorter than the time during which the layer temperature decreases by a certain value (in our experiments, ~10 s).

3. *Below a certain critical temperature in the heating region of the fluid, the droplets are unstable (it is conceivable that not the temperature but a combination of attendant thermodynamic characteristics of the evaporation process is the decisive factor).* In particular, the data obtained for a water/(ebonite substrate) system using a copper–constantan thermocouple immersed in the layer can be given as an example: (a) a fog in the convective flame appears at 43°C (air temperature ~25°C); (b) the droplets falling to the free layer surface exist for a short time (several seconds) at 46°C; (c) the droplets stabilize and form a cluster at 52°C.

4. *The layer must be open in the heating region, because the droplet stabilization occurs only in the convective flame jets.* After shutting off the cuvette with a transparent film, the hitherto stable droplets disappear simultaneously with the flame.

5. *The steam-and-air jets of the convective flame have a pronounced centripetal velocity component in the near-surface layer and serve as a driving force that directs the individual droplets and the cluster as a whole to the common center.* Following the dead zone at the center of the convective flame base, a cluster can move along the surface at distances on the order of several of its diameters without breaking its structure.

Let us discuss in greater detail the results concerning SASs. It was revealed, even at the first observations of clusters, that water samples were contaminated with SASs and showed no trace of convection. A different situation occurred with clean fluids: by the time of flame development, the layer was disturbed by the thermocapillary (TC) flows so severely that the droplets falling to it found themselves in a highly aggressive, in terms of mechanical action, medium. In fluids with a high surface tension (all the aforementioned fluids, except for butanol, can be attributed to them), where the SASs suppressed the TC effect, the layer "quieting" after the introduction of a SAS was always accompanied by droplet stabilization. However, this fact does not give the answer to the question of whether the SAS effect amounts only to quieting the layer or the role of SASs is much more complicated. Yet the fact that droplet stabilization was observed without regard to the properties and concentration of SASs (vegetable oil and hexadecanol were used) counts in favor of the first version.

For a droplet cluster, any hypothesis should reveal the cause of the (a) absence of droplet coalescence; (b) droplet stability to evaporation; and (c) ordering of the cluster structure. In this work, we propose a hypothesis based on the thermocapillary noncoalescence mechanism, which is well elaborated for relatively large droplets [3, 4]. According to this mechanism, a gas layer

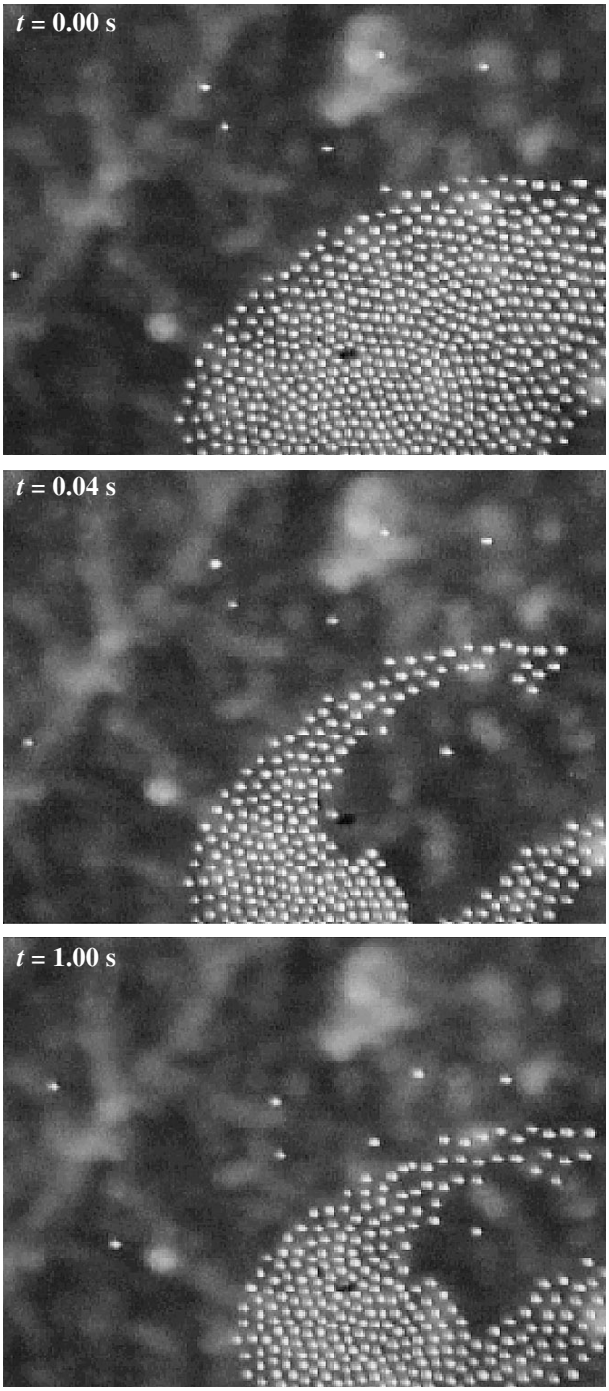

Fig. 2. Video frames of the process of disappearance of a segment in a droplet cluster. The term "disappearance" is rather pictorial because the process of droplet destruction is not detected by a video camera at a recording speed of 25 frames per second; i.e., it proceeds in a time shorter than 0.04 s.

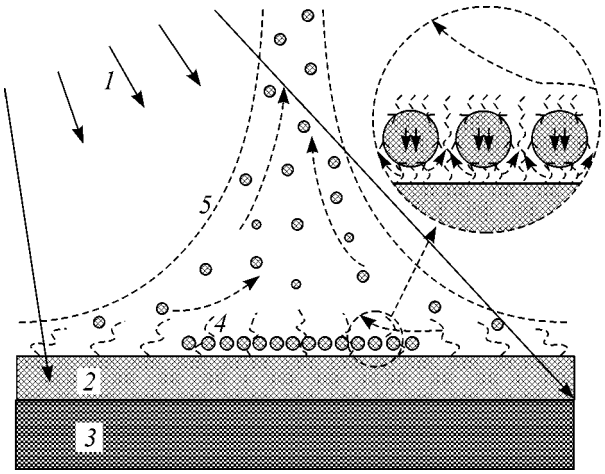

Fig. 3. Scheme of the phenomenon within the framework of the suggested hypothesis. (*1*) Light beam, (*2*) fluid layer, (*3*) substrate, (*4*) droplet cluster, and (*5*) convective flame. The dashed and solid arrows indicate the gas and fluid flows, respectively; the wavy lines indicate the steam flows.

carried away by the TC flows in a fluid prevents the coalescence of the droplet and the fluid surface, provided that the difference in their temperatures is sustained. This hypothesis suggests that intense TC flows are developed in the cluster droplets (Fig. 3) as a results of droplet heating from below and cooling from above. These flows, first, entrain the gas flows (a mixture of steam and air), which, together with the convective flame flows, form a gas blanket that prevents droplet coalescence, and, second, promote the dynamic regime, for which evaporation from the droplet top is compensated by steam condensation at the droplet bottom surface that is cooled by the paraxial fluid flow (Fig. 3). Due to the balance of steam flows, the droplets are stabilized and can exist, without changing their diameter, for many minutes at the layer surface under nonequilibrium (from the standpoint of Kelvin equation) conditions.[1] As for the cluster structure, it likely results from the action of aerodynamic flows of a different origin and, in essence, corresponds to the close packing of identical spheres on a plane.

I am grateful to Prof. D. Schwabe for support at the initial stage of the study and to A.N. Aksenov for assistance.

REFERENCES

1. G. Da Costa and J. Calatroni, Appl. Opt. **18**, 233 (1979).
2. A. A. Fedorets, Candidate's Dissertation in Physics and Mathematics (Tyumen State Univ., Tyumen, 2002).
3. P. Dell'Aversana, J. R. Banavar, and J. Koplik, Phys. Fluids **8**, 15 (1996).
4. D. Schwabe and P. Hintz, J. Non-Equilib. Thermodyn. **25**, 215 (2000).

Translated by V. Sakun

[1] The well-known equation relating the curvature of fluid surface to the steam pressure.

JETP Letters, Vol. 79, No. 8, 2004, pp. 375–380. Translated from Pis'ma v Zhurnal Éksperimental'noĭ i Teoreticheskoĭ Fiziki, Vol. 79, No. 8, 2004, pp. 460–466.

Defect Formation in a Carbon Onion upon Irradiation with Ar Ions

I. V. Ponomareva* and L. A. Chernozatonskiĭ**

Emanuel Institute of Biochemical Physics, Russian Academy of Sciences, ul. Kosygina 4, Moscow, 119991 Russia
*e-mail: *iponomar@sky.chph.ras.ru; **cherno@sky.chph.ras.ru*

Received March 1, 2004; in final form, March 5, 2004

The interaction of an Ar ion with a $C_{60}@C_{240}@C_{540}$ carbon onion and an Ar ion beam with a $C_{60}@C_{240}@C_{540}@C_{960}$ carbon onion are studied by molecular dynamics. The energy threshold for the formation of a vacancy in a pentagon of the onion fullerene shell is examined in two temperature regimes (300 and 1000 K). The main types of defects formed in the onion structure at various incident ion energies are detected and described. It is shown that the pentagonal cycles with their nearest environment are the least stable regions in the carbon onion under irradiation. The results obtained provide direct confirmation of the possibility of formation of a diamond structure upon ion irradiation of carbon onions. © *2004 MAIK "Nauka/Interperiodica"*.

PACS numbers: 61.80.Jh; 61.48.+c

The discovery of carbon fullerenes and nanotubes gave rise to a new field in the physics of atomic clusters, initially combined under the name "fullerenes and nanotubes." However, this field progressed rapidly, and it soon became evident that this definition did not reflect the whole diversity of the knowledge accumulated on these remarkable objects. This resulted in the emergence of narrower branches such as synthesis, mechanical properties, transport properties, electronic properties, and multiterminal compounds of nanotubes; later on, noncarbon nanotubes were synthesized. Quite recently, the appearance of experimental works on the irradiation of carbon onions [1, 2] and nanotubes [3] instigated the emergence of a new promising field associated with the use of electron and ion beams for changing the state, morphology, and properties of such nanoobjects. In parallel with the experimentally accumulated experience, theoretical studies of the irradiation effect on the structure of carbon onions and nanotubes were carried out [4–10].

In 1996, it was shown in [2] that the irradiation of carbon onions led to the formation of a diamond structure in their cores. Several models explaining this process were proposed [2, 8–10]. A thermodynamic model of the graphite-to-diamond transformation under nonequilibrium conditions (irradiation and temperature action) was developed in [8] and then compared with experiment on the transformation of carbon onions to diamond. This model suggests that, depending on the experimental parameters (radiation dose, beam energy, temperature, etc.), a situation can occur where graphite becomes a metastable phase and diamond, in contrast, becomes a stable phase.

In [9], it was shown by density functional theory that the formation of a $C_{60}@C_{240}$ structure containing 70 sp^3 atoms on the average in the core of a carbon onion requires the creation of nonequilibrium conditions: a considerable inflow of atoms from the outer shells into this core part of the onion (130 additional atoms) and a local increase in temperature to 2100 K. However, this value exceeds the experimental temperature by a factor of 2.5 [2]. The possible transformation stages of a carbon onion core into a diamond-like structure were considered in [10]. However, the process of bombardment of a carbon onion was not studied directly in that work.

It was shown in [3] that the irradiation of two single-walled nanotubes in the region of their contact leads to their fusing and the formation of a multiterminal junction. A molecular dynamic simulation of the interaction of an ion beam with the fusing of two single-walled nanotubes was considered in [5]. However, in spite of the rich diversity of experiments on the irradiation of carbon nanoobjects and models explaining these experiments, the study of the effect of irradiation on a graphite-like network of carbon atoms underlies these experiments. The following objects for studying the defect formation under irradiation can be distinguished in a graphite-like network of carbon atoms: (a) graphite, (b) nanotube, and (c) fullerenes and onions. The difference between these objects is mainly due to the difference in the curvature of the irradiated surface. Moreover, it is evident that the interaction of an electron or ion beam with fullerene will also differ from its interaction with a graphite plane or a perfect nanotube because of the occurrence of topological defects (pentagons) in the fullerene structure, which are responsible for the positive curvature of the surface of a fullerene molecule. Note that the effect of irradiation on graphite was stud-

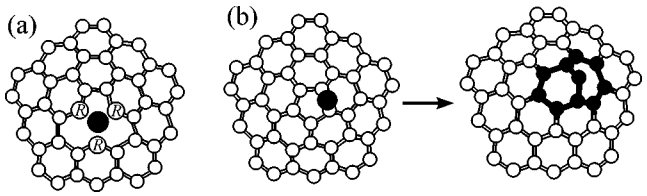

Fig. 1. Formation of a vacancy in an onion shell followed by the adsorption of the released atom by the adjacent shell. (a) Single vacancy in the onion shell. The knocked-out atom is shown by a large black circle. The radicals surrounding the vacancy are marked by *R*. (b) Adsorption of a carbon atom by the onion shell. On the left, a free atom (large black circle) is located over one of the pentagon bonds. On the right, an atom is incorporated in the shell and ruptures a bond in the pentagon. The adsorbed atom has a dangling bond.

ied in [8, 11], and the interaction of an ion beam with a carbon nanotube was considered in detail in [4–6].

The goal of this work was to study the interaction of an ion beam with a carbon onion, which represents a macromolecule composed of fullerenes differing in diameter so that the distances between them are close to the interlayer separation in graphite [12].

Bombardment of a $C_{60}@C_{240}@C_{540}$ carbon onion with Ar ions. The effect of an ion beam on a carbon onion was studied by molecular dynamics with an integration step of 0.5 fs for the equations of motion. The interatomic carbon–carbon interaction was simulated using a many-body empirical potential smoothly passing into a long-range Lennard-Jones potential at interatomic distances exceeding the cutoff radius of the empirical potential [13–15]. Such an empirical potential was previously used to simulate carbon–carbon interactions in the bombardment of single-walled nanotubes with argon ions [4–6] and electrons [16] and the bombardment of a bundle of single-walled and multi-walled nanotubes with CH_3^+ ions [7], as well as to simulate the process of ion sputtering onto polymer surfaces [17, 18]. The interaction of argon ions between each other and with carbon atoms was simulated by a Lennard-Jones potential [19]. The use of a simple repulsive potential to simulate the irradiation of carbon nanotubes with argon ions showed that it adequately describes such processes as the formation of single and cluster vacancies in the structure, a Stone-Wales-type bond rotation, and some other types of defects [4–6].

It was recently shown [4] that a single vacancy is the dominating type of defects formed in the nanotube structure upon the bombardment of single-walled carbon nanotubes. The formation threshold of such a vacancy is 50 eV. The maximum amount of the formed defects corresponds to an energy of 600 eV, then it decreases, and, starting with an energy of 1000 eV, a further increase in the ion energy does not lead to a change in the amount of defects formed in the tube. Because these data contain full information about the interaction of ions with a defect-free hexagonal network of carbon atoms, the main attention in this work was given to the interaction of ions with the atoms of pentagons in the onion structure.

In the first computational run, the $C_{60}@C_{240}@C_{540}$ carbon onion composed of three fullerene shells was bombarded with an Ar ion. One of the pentagon atoms in the outer onion shell was selected as the target for the ion. We used the onion temperature (T) and the incident ion energy (E_{in}) as the parameters of the model experiment. The Berendsen thermostat [20] was used for temperature control. In this method, the isothermal process is simulated by placing the system in a thermal bath at a constant temperature. The duration of the bombardment process with one ion was Δt = 2.5 ps. With this choice of Δt, the collision time of an ion possessing the lowest E_{in} value among the values used in the model experiment is $(1/10)\Delta t$, allowing one to trace the post-collision defect evolution.

The main tasks of the first computational run were as follows:

determination of the energy threshold for vacancy formation at the position of the target atom in the low-temperature (T = 300 K) and in the high-temperature (T = 1000 K) regimes;

determination of the main types of defects initiated by vacancy formation in the onion structure.

Low-temperature regime: onion temperature 300 K. In the first model experiment (ME), the incident ion energy E_{in} was 40 eV. In each subsequent ME, we increased the incident ion energy by 10 eV. It was found that defects were formed in the structure of the onion fullerene shells starting with an energy of 100 eV. At this value of energy E_{in}, the target atom is knocked out, and a vacancy surrounded by three radicals is formed in the outer-shell structure (Fig. 1a). The knocked-out carbon atom (a large black atom in Fig. 1) is adsorbed by the adjacent onion shell. This atom ruptures one of the bonds in a pentagon of the adjacent shell to incorporate into it (Fig. 1b). This process is similar to the adsorption process described in [21]. Note that the equilibrium onion state corresponds to such an arrangement of its shells at which pentagons in different shells are located under each other [10].

At E_{in} = 110 eV, the target atom is knocked out of the pentagon; however, only two of its three bonds are ruptured. The outer-shell atom to which the target atom is bound is displaced toward the depth of the onion, so that the only bond of the target atom is now directed along the onion radius.

Thus, at T = 300 K, the energy threshold for vacancy formation at the position of the target atom is 100 eV.

High-temperature regime: onion temperature 1000 K. Based on the results of the preceding step, we started calculations with the energy E_{in} equal to 110 eV and decreased it by 10 eV at each subsequent step.

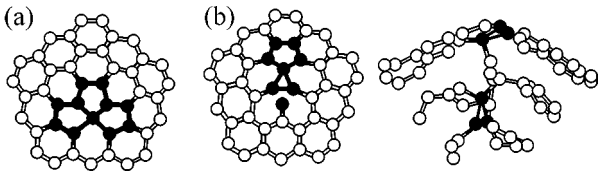

Fig. 2. Examples of defects formed in the onion upon its bombardment with Ar ions. (a) A defect with a four-coordinate atom at the center formed as a result of the rearrangement of radicals (*R*) in Fig. 1a. (b) A group of bonded defects formed in the onion at $T = 1000$ K and at $E_{in} = 80$ eV. On the left, a defect in the outer shell is shown; on the right, three onion shells are bonded together (triangular cycles of atoms are marked by dark shade).

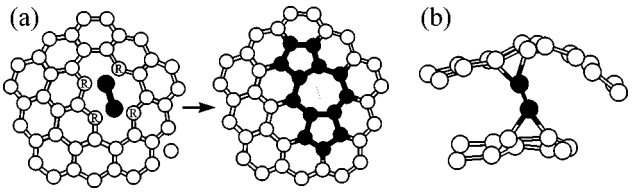

Fig. 3. A defect formed in the onion at $T = 1000$ K and at $E_{in} = 60$ eV. (a) On the left, a dimer knocked out of the outer shell is shown in black; radicals surrounding a double vacancy are designated by R. On the right, the recombination of radicals is shown; as a result, two pentagons and a heptagon are formed (shown in dark). (b) A knocked-out dimer that bonds two shells is shown in dark.

At $E_{in} = 110$ eV, the ion knocks out the target atom, which is adsorbed by the adjacent shell, as is shown in Fig. 1b, to form simultaneously a bond with an outer-shell atom. Two of the three atoms with dangling bonds recombine to create a pentagon [22].

The incident ion with an energy of 100 eV knocks out the target atom, which is then adsorbed by the adjacent shell (see Fig. 1b). The rearrangement of atoms surrounding the vacancy formed in the outer shell gives rise to a defect shown in Fig. 2a. An atom with the coordination number CN = 4 is located at the center of this defect. A four-coordinate atom in the vicinity of the vacancy can also be formed in the hexagonal network. In this case, such an atom is simultaneously a vertex of two pentagons and two hexagons [22].

The target atom knocked out of the outer onion shell by the incident ion with energy $E_{in} = 90$ eV behaves in a different way. Again, a vacancy surrounded by three radicals (Fig. 1a) is formed at the position of this atom after the interaction with ion. Two of these radicals subsequently recombine to form a pentagon. Next, the target atom knocks out one of the atoms of the adjacent shell and occupies its position. The atom released in this process is adsorbed by the inner C_{60} shell.

A complicated cascade of defects in the onion structure is formed at the ion energy $E_{in} = 80$ eV. The defect in the outer shell is shown in Fig. 2b on the left. A radical in the outer shell (see the left part of Fig. 2b) forms a bond with atoms of the adjacent shell. The target atom is adsorbed by the adjacent shell, knocks an atom out of it, and instigates the formation of defects in this shell that are a combination of the elementary defects shown in Figs. 2 and 3a. The complicated trajectory of the target atom knocked out of the outer shell results in the mutual bonding of all three shells (Fig. 2b, right). The presence of two triangles (see Fig. 2b) is also a characteristic feature of such a structure.

At the ion energy $E_{in} = 70$ eV, the target atom is also incorporated into the adjacent shell through knocking out one of its atoms, which is subsequently adsorbed by the inner shell. However, this atom, being incorporated into the inner shell, ruptures one of the bonds of a hexagon (rather than pentagon, as in Fig. 1b), giving rise to two heptagons instead of two hexagons. It should be noted that the adsorbed atom in this mechanism bears a dangling bond, which is oriented in the direction from the center of the onion. Such a configuration is characterized by extremely high reactivity, which leads, in this particular case, to the formation of a chemical bond with an atom of the adjacent central shell. As a result, this atom of the adjacent shell occurs in the sp^3 state.

At the next step, the ion energy was 60 eV. A dimer is knocked out of the bombarded pentagon. The occurrence of dangling bonds at four atoms (Fig. 3a, left) surrounding the vacancy, whose saturation gives rise to two pentagons and one heptagon (Fig. 3a, right), is a consequence of the formation of a double vacancy. The axis of the knocked-out dimer is oriented along the onion radius, because of which it connects the outer and middle shells (Fig. 3b). An sp^3 bond between the atoms of the inner and middle shells is also formed not far from the main defect.

At $E_{in} = 50$ eV, the target atom is not knocked out of the bombarded pentagon; however, it is strongly displaced inward the onion, leading to the rupture of one of its bonds. Thus, two radical atoms arise in the outer onion shell. One of them (the target atom), gaining a momentum from the Ar ion, is displaced inward, leading to its bonding to an atom of the adjacent shell. The other one is displaced in the opposite direction. Next, the cascade of defects in the onion develops according to the following scenario: the middle-shell atom bonded now to the target atom is displaced outward the center of the onion, leading to the rupture of one of its bonds. As a result, a radical forms in the structure of the middle shell. This radical is displaced toward the center of the structure and forms a bond with one of the atoms of the inner shell. As a result, this atom becomes tetrahedrally coordinated. Thus, the incident ion with an energy of 50 eV gives rise to a cascade of defects of the same type in the onion shells. It is evident that the ion energy in this case is insufficient for the target atom to be knocked out of the shell. The energy and momentum gained as a result of collision go into the bond rupture

Distribution of carbon atoms (N_{at}) in the coordination number CN in a $C_{60}@C_{240}@C_{540}$ onion for different temperature regimes (T = 300 K and T = 1000 K) after the bombardment by an Ar ion with energy E_{in}

		T = 300 K			T = 1000 K									
K	E_{in}	90 eV	100 eV	110 eV	20 eV	30 eV	40 eV	50 eV	60 eV	70 eV	80 eV	90 eV	100 eV	110 eV
1	N_{at}	0	0	1	0	0	0	0	0	0	0	0	0	0
2		0	4	0	0	0	0	1	0	0	1	1	1	1
3		840	836	837	840	838	840	838	834	836	832	838	838	838
4		0	0	2	0	2	0	1	6	4	7	1	1	1

and the displacement of the resulting radicals in the opposite directions from each other. It should be noted that this cascade mechanism of defect formation is extremely productive for the binding of onion shells.

At E_{in} = 40, 30, and 20 eV, vacancies in the onion shell do not form. Note that, at energies as low as those, the target atom is often displaced inward, leading to the formation of an sp^3 bond with an atom of the adjacent shell.

The distribution of atoms in the coordination number is given in the table for different energies of the Ar ion. It is seen from the table that the maximum number of atoms with CN = 4 in the high-temperature regime corresponds to an incident ion energy of 60–80 eV.

Thus, it is found in this computational run that the energy threshold for vacancy formation at the position of the target atom depends on temperature and equals 100 eV at T = 300 K and 60 eV at T = 1000 K. At low ion energies (20–40 eV), sp^3 bonds are formed between the outer shells.

Note that not all the possible types of defects but only the most frequently occurring ones are described above.

Bombardment of a $C_{60}@C_{240}@C_{540}@C_{960}$ carbon onion with an Ar ion beam. In contrast to a perfect nanotube, not all atoms in fullerene are equivalent with respect to the ion beam because of the occurrence of topological defects in the form of pentagons in the structure. To reveal the distinctions between the interactions of onion atoms belonging to pentagons and hexagons, we carried out the following experiment with incident ions: the surface of a $C_{60}@C_{240}@C_{540}@C_{960}$ carbon onion consisting of four shells was irradiated with an Ar ion beam. We increased the number of shells in the onion by one, compared to the preceding step, in order to increase the area of ion-beam interaction with the onion. The ratio of the cross-section area of the incident beam to the maximum cross-section area of the onion was ~1.1. The irradiation dose was 0.5×10^{15} ion/cm^2. For this dose, the minimum distance between Ar ions in the beam was 4.5 Å. Therefore, according to the chosen potential, these ions may be considered as weakly interacting with each other. The ratio of the incident beam mass to the onion mass was 0.09, as a result of which there was no necessity of modeling the substrate to compensate the momentum of the incident beam. The duration of one ME was Δt = 10 ps. We increased Δt by a factor of 4 compared to the preceding step. Because the number of defects in the structure increases with increasing number of incident ions, the defect evolution now has a collective character, leading to an increase in the equilibration time for the structure.

Low-temperature regime: onion temperature 300 K. Within this step, we performed three computational runs in the low-temperature regime (T = 300 K) for ion energies in the beam equal to 0.1, 0.5, and 1.0 keV. In each computational run, 12 MEs were carried out for different orientations of the onion about the beam. The onion was rotated 90° about each principal axis of inertia, the beam direction being perpendicular to this particular axis.

The formation of an sp^3 bond between two outer shells is the main type of defects in the structure at an ion energy of 0.1 keV in the beam. We observed the formation of a vacancy in a pentagon only in one ME. The irradiation-induced bond rupture between two pentagon atoms was also observed in only one ME. Vacancies in hexagons do not form at this ion energy.

At an energy of 0.5 keV, the bonding of the outer shells through the sp^3 bonds is also the most frequently occurring type of defects. However, single vacancies in five-membered cycles were formed in 3 of 12 MEs. The vacancy formation in hexagons was not observed for the given ME parameters.

Upon the irradiation of the onion by an ion beam with an energy of 1 keV, the number of vacancies increases drastically. The position of hexagons relative to pentagons in C_{960} fullerene can be characterized using the following terminology: the hexagons immediately adjacent to a pentagon will be called the first pentagon coordination sphere (PCS), and the hexagons next to these hexagons will be called the second PCS. Thus, each pentagon in the C_{960} fullerene has three PCSs (shown in the inset in Fig. 4). The pentagon itself will be called the zeroth PCS. In the graph in Fig. 4, crosses show the distribution of the relative number of vacancies over the PCSs. The graph demonstrates that the distribution maximum corresponds to the first coordination sphere.

High-temperature regime: onion temperature 1000 K. We carried out analogous calculations for the high-temperature regime. The distribution of atoms over the PCSs is represented in Fig. 4. The graph demonstrates that the maximum number of vacancies is formed at pentagon atoms for all three ion energies in the beam used in this study. As the general tendency, it should be noted that the number of formed vacancies decreases as the PCS number increases, i.e., as the distance from the pentagon increases. For an ion energy of 1 keV, cluster vacancies are also formed [4], and all pentagon atoms are knocked out for certain beam orientations about the onion. At energies of 0.5 and 1 keV, the knocked-out carbon atoms possess an energy sufficient for the formation of vacancies in the inner onion shells. The maximum penetration depth of defects in the onion is equal to two shells for ion energies of 0.1 keV and three shells for ion energies of 0.5 keV, whereas all four onion shells are damaged at ion energies of 1 keV.

The main conclusions of this computational step are as follows:

for the chosen ion energies in the beam and chosen irradiation dose, the maximum number of vacancies are formed in pentagons, and the number of the formed vacancies decreases as the distance from the pentagon regions increases;

the defect penetration depth increases as the beam energy increases;

at high ion energies in the beam, cluster vacancies are formed, and vacancies are formed in the pentagons of the adjacent shells located under the pentagon with primary vacancies.

Thus, it is shown in this work that, in the case of a uniform irradiation of a carbon onion with an ion beam, the probability of vacancy formation is distributed nonuniformly over the onion surface. It decreases as the distance from the pentagon regions increases. The energy threshold for the vacancy formation in a pentagonal cycle depends on temperature and decreases with increasing temperature. The formation of a bond between two neighboring radicals in the shell and the formation of intershell bonds are the main routes for the saturation of bonds formed by radical atoms surrounding the vacancy. As a result of the latter process, sp^3 atoms can arise in the onion structure. An alternative mechanism for the formation of sp^3 atoms consists in the displacement of the shell atoms upon the collision with an ion of the adjacent shell. In the majority of cases, the carbon atom released as a result of collision is adsorbed by the adjacent shell if one of its interatomic bonds is ruptured. The knocked-out atom itself can be the source of vacancy formation in the adjacent shells. A vacancy in an onion shell has a short lifetime ($T_{life} < 2.5$ ps). On the whole, the bombardment of a carbon onion with an ion beam leads to the formation of a considerable number of topological defects in its structure in the form of pentagons and heptagons. The three-membered cycles arise in the structure less frequently.

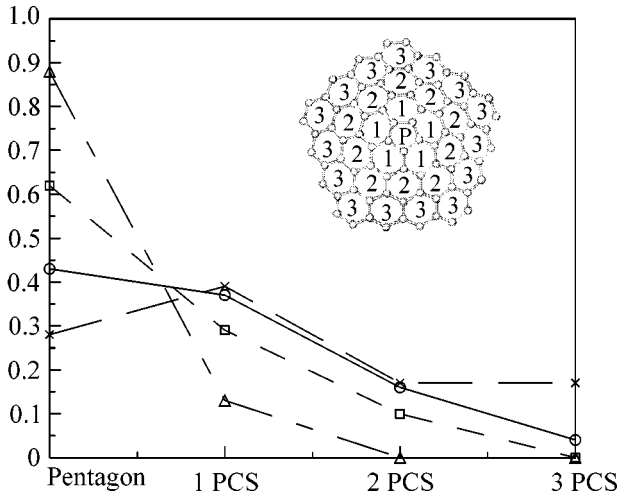

Fig. 4. Distribution of the relative number of vacancies over the pentagon coordination spheres. The ratio of the number of vacancies in a particular PCS to the total number of vacancies in all PCSs is plotted on the ordinate axis. Crosses mark the results of simulation at $T = 300$ K and $E_{in} = 1$ keV; triangles correspond to $T = 1000$ K and $E_{in} = 0.1$ keV; squares correspond to $T = 1000$ K and $E_{in} = 0.5$ keV; and circles correspond to $T = 1000$ K and $E_{in} = 1$ keV.

It is shown on the atomic level that the bombardment of a carbon onion with Ar ions leads to the bonding between its shells and to the formation of sp^3 atoms at relatively low temperatures, which directly confirms the possibility of a carbon onion transformation to diamond under irradiation [1, 2].

This work was supported by the project "Fullerenes and Atomic Clusters" of the Russian program "Topical Directions in the Physics of Condensed Matter."

REFERENCES

1. P. Wesolowskii, Y. Lyutovich, F. Banhart, *et al.*, Appl. Phys. Lett. **71**, 1948 (1997).
2. F. Banhart and P. M. Ajayan, Nature **382**, 433 (1996).
3. M. Terrones, F. Banhart, N. Grobert, *et al.*, Phys. Rev. Lett. **89**, 075505 (2002).
4. I. V. Krasheninnikov, K. Nordlund, M. Sirviö, *et al.*, Phys. Rev. B **63**, 245405 (2001).
5. A. V. Krasheninnikov, K. Nordlund, and J. Keinoneon, Phys. Rev. B **66**, 245403 (2002).
6. A. V. Krasheninnikov, K. Nordlund, and J. Keinoneon, Phys. Rev. B **65**, 165423 (2002).
7. B. Ni, R. Andrews, D. Jacques, *et al.*, J. Phys. Chem. B **105**, 12719 (2001).
8. M. Zaiser and F. Banhart, Phys. Rev. Lett. **79**, 3680 (1997).
9. R. Astala, M. Kaukonen, and R. M. Nieminer, Phys. Rev. B **63**, 081402 (2001).

10. I. V. Ponomareva and L. A. Chernozatonskiĭ, Pis'ma Zh. Éksp. Teor. Fiz. **76**, 532 (2002) [JETP Lett. **76**, 456 (2002)].
11. T. L. Daulton, M. A. Kirk, R. S. Lewis, and L. E. Rehn, Nucl. Instrum. Methods Phys. Res. B **175–177**, 12 (2001).
12. D. Ugarte, Nature **359**, 707 (1992).
13. D. W. Brenner, O. A. Shendorova, J. A. Harrison, *et al.*, J. Phys.: Condens. Matter **14**, 783 (2002).
14. D. W. Brenner, Phys. Status Solidi B **217**, 23 (2000).
15. S. Sinnott, O. A. Shendorova, C. T. White, and D. W. Brenner, Carbon **36**, 1 (1998).
16. I. Jang, S. B. Sinnott, D. Danailov, and P. Keblinski, Nano Lett. **4**, 109 (2004).
17. M. B. J. Wijesundara, Y. Ji, B. Ni, *et al.*, J. Appl. Phys. **88**, 5004 (2000).
18. M. B. J. Wijesundara, L. Hanley, B. Ni, and S. B. Sinnott, Proc. Natl. Acad. Sci. USA **97**, 23 (2000).
19. G. C. Maitland, M. Rigby, E. B. Smith, and W. A. Wakeham, *Intermolecular Forces: Their Origin and Determination* (Clarendon, Oxford, 1981).
20. H. J. C. Berendsen, J. P. M. Postma, W. F. van Gunsteren, *et al.*, J. Chem. Phys. **81**, 3684 (1984).
21. K. Nordlund, J. Keinoneon, and T. Mattila, Phys. Rev. Lett. **77**, 699 (1996).
22. P. M. Ajayan, V. Ravikumar, and J.-C. Charlier, Phys. Rev. Lett. **81**, 1437 (1998).

Translated by A. Bagatur'yants

JETP Letters, Vol. 79, No. 8, 2004, pp. 381–382. Translated from Pis'ma v Zhurnal Éksperimental'noĭ i Teoreticheskoĭ Fiziki, Vol. 79, No. 8, 2004, pp. 467–469.

Formation of Silver Nanodots and Nanowires on a Si(557) Surface

R. A. Zhachuk, S. A. Tiĭs, and B. Z. Ol'shanetskiĭ*

Institute of Semiconductor Physics, Siberian Division, Russian Academy of Sciences, Novosibirsk, 630090 Russia

**e-mail: olshan@isp.nsc.ru*

Received March 16, 2004

Scanning tunneling and Auger spectroscopy were used to study the formation of silver nanostructures at room temperature on a Si(557) surface containing regular atomic steps with a height of three interplanar spacings. The shape of silver islands formed on the surface was found to be affected by oxygen adsorbed on the silicon surface from the residual atmosphere in a vacuum chamber. Depending on the amount of adsorbed oxygen, silver nanostructures can be obtained in the form of nanowires extended along the edges of steps or nanodots ordered in lines parallel to these edges. © *2004 MAIK "Nauka/Interperiodica".*

PACS numbers: 68.65.Hb; 68.65.La; 68.37.Ef; 68.47.Fg

In the last few years, considerable interest has been attracted to the formation of low-dimensional structures of the quantum-dot and quantum-wire types on silicon surfaces. However, the number of systems that allow the formation of nanostructures with the properties necessary for the manifestation of quantum-dimensional effects is limited [1–5]. The use of high-index surfaces as substrates may facilitate the ordering of growing structures.

In this paper, we report the formation of silver nanodots and nanowires on a Si(557) surface. This vicinal surface is inclined with respect to the (111) plane at an angle of 9.45° in the $[\overline{1}12]$ direction. At temperatures below 870°C, the steps formed on the surfaces inclined in this direction have heights equal to one and three interplanar spacings d_{111} [6–8]. As the angle of inclination increases, the proportion of steps with a height of $3d_{111}$ increases, while the proportion of steps with a height of $1d_{111}$ decreases [8]. The Si(557) surface contains only steps with a height of $3d_{111}$ [9].

It was established that the shape of growing silver islands depends on the duration of preexposure of a clean silicon surface in vacuum.

Figure 1 shows the Si(557) surface image obtained with a scanning tunneling microscope (STM) after four silver MLs (ML denotes monolayer) were deposited on the sample at room temperature immediately after the surface was cleaned. One can see sparse islands covering several Si(111) terraces. The islands are widely scattered in size and chaotically distributed over the surface. Figure 2 shows the Si(557) surface on which four silver MLs were deposited at room temperature after a 15-min preexposure of the sample in a vacuum chamber under a pressure of 5.0×10^{-10} mmHg. One can see an array of silver nanowires on the surface and also sparse silver islands on two or more Si(111) terraces. When six silver MLs were deposited on the sample, nanowires up to 150 nm long were obtained, their width being approximately 5 nm. Figure 3 shows the STM image of the Si(557) surface after a two-hour exposure in the vacuum chamber at 5.0×10^{-10} mmHg and a subsequent deposition of two silver MLs. This surface contains an array of dotlike islands. The nanodots formed in this way are ordered in lines parallel to the edges of triple steps, because they lie on the Si(111) terraces. The lateral size of nanodots is limited by the width of Si(111) terraces, and, hence, the nanodots are characterized by a relatively small scatter in size.

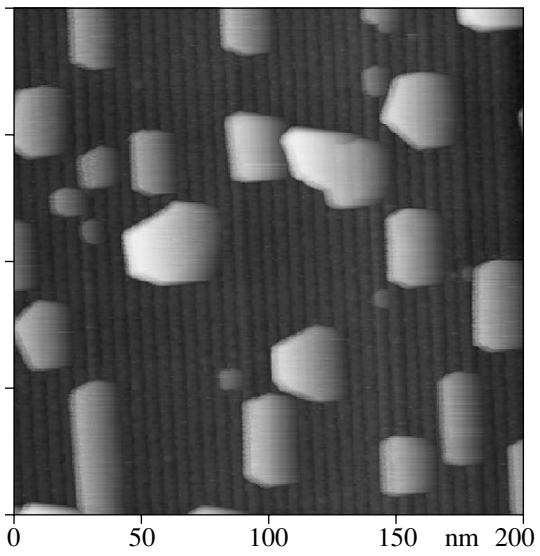

Fig. 1. STM image of a Si(557) surface containing four silver MLs.

0021-3640/04/7908-0381$26.00

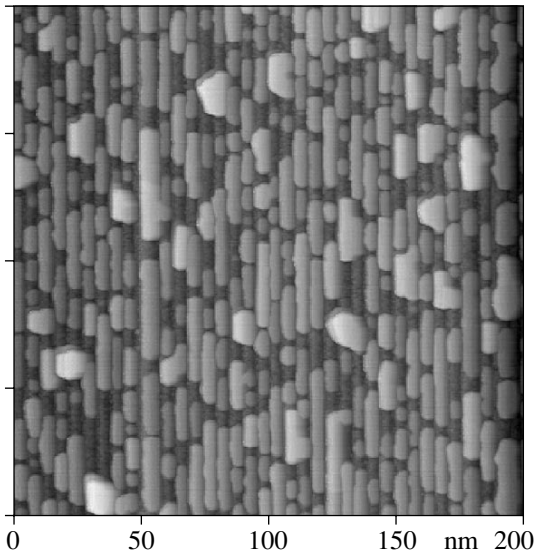

Fig. 2. Silver nanowires formed on the Si(557) surface after the adsorption of 0.003 ML of oxygen and the deposition of 4 silver MLs.

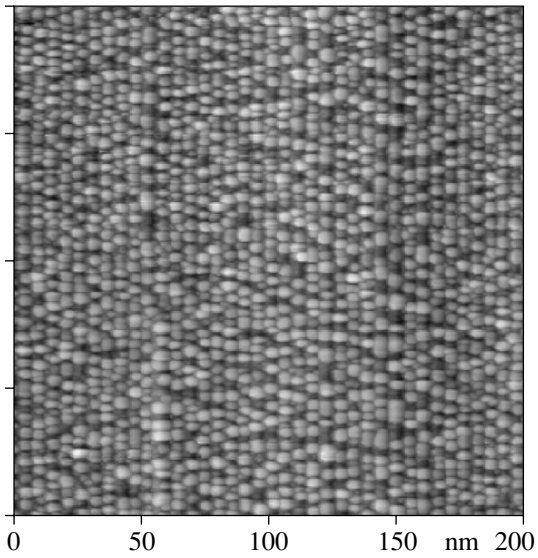

Fig. 3. Silver nanodots formed on the Si(557) surface after the adsorption of 0.025 ML of oxygen and the deposition of 2 silver MLs.

The adsorption of impurities from residual gases onto the substrate surface is the evident cause of the influence of the preexposure in a vacuum chamber on the shape of silver islands. According to the Auger data, after a clean silicon surface was held at a residual gas pressure of 1.6×10^{-10} mmHg for 24 h, the spectra obtained from the Si(111) surface showed the presence of only the oxygen impurity with a content corresponding to 0.06 oxygen MLs. On the Si(557) surface, the oxygen content was higher and corresponded to 0.095 MLs, which is presumably caused by the fact that the probability of oxygen adhesion at the edges of triple steps is higher than at Si(111).

The concentration of oxygen adsorbed on the surface is proportional to the exposure $p \times t$, where p is the pressure of residual gases in the vacuum chamber and t is the time of exposure, provided that this concentration is small. Therefore, it is possible to estimate the oxygen concentrations necessary for the formation of arrays of silver nanowires and nanodots on the Si(557) surface. For the nanowire array shown in Fig. 2, the oxygen concentration was equal to 0.003 ML, and for the nanodot array in Fig. 3, 0.025 ML.

Oxygen adsorbed on the surface plays the role of a surfactant [10] that governs the shape of the growing silver islands. A possible mechanism of this effect can be as follows. Oxygen atoms adsorbed on the surface close the silicon dangling bonds and, hence, lead to a change in the free energy of the surface. As a result, parts of the silicon surface that are covered with oxygen cease to be wetted with silver. Thus, oxygen forms a mask for the silver adsorption on the silicon surface. In the case of short exposures, oxygen is predominantly incorporated into the edges of triple steps on the Si(557) surface, and, hence, silver nanowires are formed on the Si(111) terraces. In the case of long exposures, oxygen is also adsorbed on the Si(111) terraces, resulting in the formation of silver nanodots.

Thus, using the Si(557) surface as the substrate, it is possible to obtain ordered arrays of silver nanostructures of nanowire or nanodot type, depending on the amount of adsorbed oxygen.

This work was supported by the Russian Foundation for Basic Research and the Ministry of Science, Industry, and Technology of the Russian Federation.

REFERENCES

1. O. G. Schmidt, S. Kiravittaya, Y. Nakamura, *et al.*, Surf. Sci. **514**, 10 (2002).
2. O. P. Pchelyakov, Yu. B. Bolkhovityanov, A. V. Dvurechenskii, *et al.*, Thin Solid Films **367**, 75 (2000).
3. H. Omi and T. Ogino, Phys. Rev. B **59**, 7521 (1999).
4. M. Jalochowski and E. Bauer, Surf. Sci. **480**, 109 (2001).
5. I. K. Robinson, P. A. Bennett, and F. J. Himpsel, Phys. Rev. Lett. **88**, 096104 (2002).
6. V. I. Mashanov and B. Z. Ol'shanetskiĭ, Pis'ma Zh. Éksp. Teor. Fiz. **36**, 290 (1982) [JETP Lett. **36**, 355 (1982)].
7. B. Z. Olshanetsky and S. A. Teys, Surf. Sci. **230**, 184 (1990).
8. Jian Wei, X.-S. Wang, J. L. Goldberg, *et al.*, Phys. Rev. Lett. **68**, 3885 (1992).
9. A. Kirakosian, R. Bennewitz, J. N. Crain, *et al.*, Appl. Phys. Lett. **79**, 1608 (2001).
10. C. Y. Fong, M. D. Watson, L. H. Yang, and S. Ciraci, Modell. Simul. Mater. Sci. Eng. **10**, R61 (2002).

Translated by E. Golyamina

JETP Letters, Vol. 79, No. 8, 2004, pp. 383–387. From Pis'ma v Zhurnal Éksperimental'noĭ i Teoreticheskoĭ Fiziki, Vol. 79, No. 8, 2004, pp. 470–474.

Metastability and Superfluid Fraction of the A-like and B Phases of ^{3}He in Aerogel in Zero Magnetic Field¶

E. Nazaretski[1], N. Mulders[2], and J. M. Parpia[1, *]

[1] *Laboratory of Atomic and Solid State Physics, Cornell University, Ithaca, NY 14853, USA*

[2] *Department of Physics and Astronomy, University of Delaware, Newark, DE 19716, USA*

**e-mail: jmp9@cornell.edu*

Received March 18, 2004

We report the low-frequency sound measurements of the metastable A-like (A*) phase of superfluid ^{3}He confined within a 98% open aerogel matrix in zero magnetic field. The second soundlike (slow) mode provides an accurate determination of the superfluid fraction of (and the transition between) the A* and B phases. The A* and B phases exhibit stable coexistence in the presence of disorder, the ratio of their superfluid fractions ($\rho_a^{A^*}/\rho_s^B$) is much smaller than that of the bulk A and B phases, and argues that the A* and bulk A phases are distinct. © *2004 MAIK "Nauka/Interperiodica".*

PACS numbers: 67.57.Bc; 64.60.My

^{3}He is an ultrapure system that undergoes a transition from a normal Fermi liquid to the *p*-wave paired superfluid state. Strong confinement of ^{3}He within regular geometries of characteristic size $\sim\xi_0$ (the superfluid ^{3}He coherence length) had been predicted to significantly alter the bulk phase diagram [1], but this was never manifested in any experiments. The introduction of silica aerogel, a network of a few nm diameter SiO_2 strands, with fractal correlations of a few to 100 nm [2] provides a route by which superfluid ^{3}He can experience correlated disorder because ξ_0 is larger than the strand diameter and of the same order of magnitude as the correlations.

The introduction of disorder also significantly alters the resulting phase diagram [3–6] beyond suppressing the superfluid transition temperature, T_{ca}. Recent work finds that a metastable A-like phase appears in both zero and finite magnetic fields, the polycritical point vanishes and the A $\longrightarrow$ B transition, T_{AB} and T_{ca} exhibit a width (partially attributed to temperature control and thermometry) [4, 7]. T_{AB} was explored in strong magnetic fields [8]; low-field NMR results definitively identified a hysteretic A $\longleftrightarrow$ B transition at high pressure [9] and identified the equilibrium low-temperature phase of ^{3}He in aerogel as the B phase [10]. However, there is controversy as to the metastability of the A-like phase in zero field [7, 11]. The only other *p*-wave paired system, the heavy fermion UPt_3, has a rich phase diagram that is modified by both pressure and magnetic fields [12], though the influence of disorder (other than the suppression of T_c) by elastic scattering [13] has yet to be mapped. Thus, there is an incomplete understanding of the effects of disorder on the phase diagrams of unconventionally paired systems.

Theoretical effort to understand the role of disorder has concentrated on the B phase [14, 15]. Only very recently, work by Fomin [16, 17], drawing on earlier general results of Volovik [18], *specifically excludes* the A phase as a stable phase in the presence of disorder and proposes other equal spin paired states as candidates for the A-like (A*) phase. However, properties that distinguish A* states from the A phase are not explicitly identified.

The A* superfluid phase that is initiated when cooling from the normal state exhibits a variety of time-dependent behavior (in magnetic fields) quite different from that of bulk A to B phase conversion. A negative frequency shift (usually associated with the ^{3}He A phase) and a positive frequency shift (associated with the B phase) were observed to be simultaneously present while cooling by Barker *et al.* [9] and the Moscow group [19]. For aerogel preplated with ^{4}He, the weight of A* decreased continuously over a broad temperature range [19] before abruptly vanishing below a temperature, T_{A^*B} [9, 19]. The results are different without ^{4}He preplating. The A* phase was unstable with a lifetime that decreased depending on the proximity to T_{A^*B} [19]. Pinning [11] has been invoked to explain the finite thermal and temporal width of the A* $\longrightarrow$ B conversion process, in contrast to bulk ^{3}He, where once initiated, the A $\longrightarrow$ B transition proceeds rapidly to completion.

The superfluid fraction, ρ_s/ρ, measured with both torsional oscillators [5, 20] and sound [21] is signifi-

¶ This article was submitted by the authors in English.

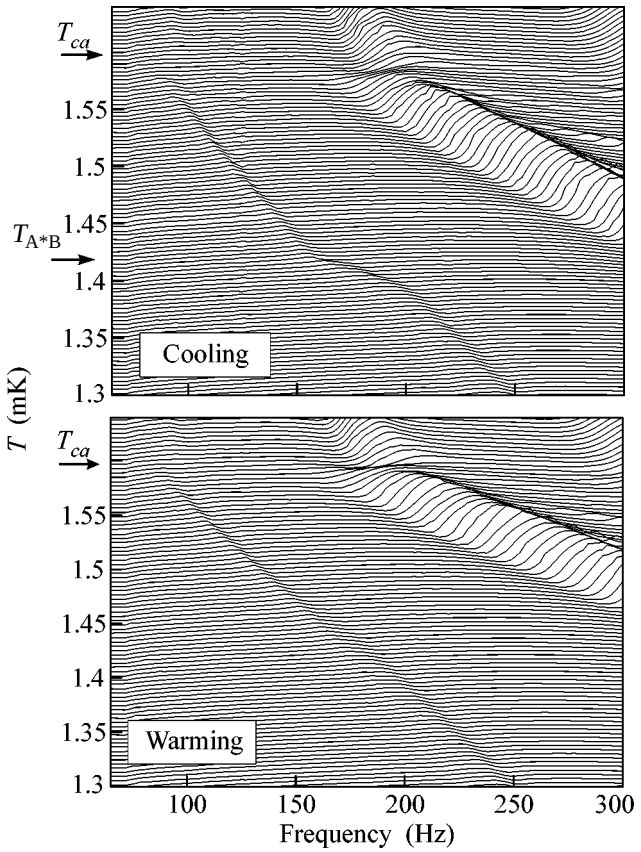

Fig. 1. Slow mode (SM) spectra at 21.01 bar offset vertically by temperature (the ordinate displays temperature and the received signal). The positive peak that merges into the weak "edge mode" below 100 Hz at T_{ca} = 1.585 mK is the fundamental SM resonance [21]. The broad feature above 170 Hz is a Helmholtz mode combined with SM harmonics that cross close to T_{ca}. The upper panel shows the evolution of the SM on cooling with the A* ⟶ B transition at T_{A*B} = 1.415 mK. The lower panel depicts the SM behavior on warming.

cantly suppressed from unity as $T \longrightarrow 0$. However, the A* phase superfluid density, ρ_s^{A*} has not been measured to date in zero field [5, 20, 21], because data were always obtained on warming after entering the B phase (due to temperature control difficulties while cooling).

In this letter, we report on zero-field low-frequency sound measurements as a function of temperature and pressure. Zero-field results are significant because of their lack of time dependence and also because the characteristic fields that alter the phase diagram and orient textures of superfluid ^{3}He can be quite small. The magnetization of the surface ^{3}He that may affect the time dependence is also field-dependent. In our experiments, the stability (*no time dependence*) of the A* and B phases and mixtures of these phases against conversion to the B phase allows us to reliably evaluate ρ_s. The sequence of phase transitions observed during warming and cooling show the following:

(1) The A* and B phases can coexist in a long-lived metastable state.

(2) The ratio of the A* and B phase superfluid fractions ρ_s^{A*}/ρ_s^B is very different from the bulk ρ_s^A/ρ_s^B. This ratio will be useful in establishing the nature of the A* phase.

(3) The transitions from A* to B (cooling) and B to normal (*N*) (warming) have widths of 20 and 25 μK, respectively, and could be partially penetrated to produce coexistent A* and B phases after warming from T_{A*B} or cooling from T_{ca}. The A* phase reproducibly supercools below T_{ca} before conversion to the B phase along a smooth curve T_{A*B} on the *PT* diagram.

The experimental cell's cylindrical aerogel filled resonator has length l = 1.64 cm and diameter d = 1.27 cm. Sound is coupled to and from the ^{3}He via piezoceramic wafers attached to coin silver "speaker" and "microphone" membranes that are in contact with the 98% open aerogel sample's ends [22]. The spectrum of the acoustic resonator from which the sound velocities can be obtained is determined by sweeping the excitation frequency. A susceptibility thermometer monitored the ^{3}He temperature, and a ^{3}He melting curve thermometer monitored the $PrNi_5$ demagnetization stage.

For a superfluid in the interstices of a compliant solid such as aerogel, the interpenetrating normal and superfluid components [23] move in phase with the aerogel to give rise to a first soundlike "fast" mode whose frequency is continuous across the superfluid transition. The onset of the "slow" mode (SM) (in which ρ_s and ρ_n move out of phase) analogous to fourth sound in rigid porous media or second sound in the bulk is the signature of superfluidity. These modes were first observed by McKenna *et al.* [24] for ^{4}He in aerogel, and the B phase modes were mapped (on warming) in ^{3}He by Golov *et al.* [21]. The SM velocity is used to determine ρ_s/ρ.

Examples of the SM's evolution while cooling (upper panel) and warming (lower panel) at 21.01 bar are shown in Fig. 1. The A* ⟶ B transition (width ~20 μK) is seen in the cooling trace and its onset, T_{A*B}, and the superfluid transition T_{ca} are marked with arrows. For $T \geq T_{ca}$, the SM converts into the "edge mode" that involves counterflow of the normal fluid in the aerogel and the layer of bulk superfluid ^{3}He around the aerogel [21]. Similar features were noted at all pressures between 28.6 and 13.16 bar and used to map out the phase diagram (Fig. 2).

In contrast to bulk ^{3}He, where the A phase is the equilibrium high-pressure, high-temperature phase and vanishes below the polycritical point (~21 bar, see Fig. 2), our studies show no evidence for a B ⟶ A* transition (in agreement with [3, 4]). Unless the B phase

superheats (unlike the bulk), it is likely that there is no region where the A* phase is the lowest free-energy (equilibrium) phase in zero magnetic field. T_{A*B} was observed down to 13.16 bar and has marked similarities to the bulk ^{3}He results of Schiffer *et al.* [25] obtained with ultraclean surfaces (Fig. 2). In traversing T_{A*B}, we varied the cooling rates between 9.5 and 100 μK/h with no effect on T_{A*B} or the transition's width (~20 μK), and T_{A*B} reproduces precisely upon cycling above T_{ca}.

NMR features have characteristics of a combination of A and B phases [9, 19], but their coexistence cannot be studied in zero field. Brussaard *et al.* [8] showed that the A* ⟶ B transition could be arrested and reversed by altering the magnetic field. We show evidence for the metastable coexistence of the A* and B phases of ^{3}He in aerogel in zero magnetic field (Fig. 3). The upper and the lower traces represent the resonant frequency in the B and A* phases, respectively. The intermediate trace was obtained by cooling into the T_{A*B} band by only ~7 μK (i.e., not traversing the transition to completion). Following this partial transition, the sample was warmed to just below the T_{ca} band (defined below) and cooled while taking data. The frequency followed a path intermediate between that of the A* and B phases, implying a partial conversion from A* to the B phase. The coexistence of the A* and B phases in aerogel is evidence for strong pinning of the A*–B interface. The mixed state (without preplating with ^{4}He) was stable at any temperature (including within 5 μK of T_{A*B} for a period of a day), in contrast to the Moscow group's findings [19] of instability for pure ^{3}He, or a broad transition for ^{4}He covered surfaces (both in a magnetic field). The stability against conversion of coexistent A* to B phases in our experiment is similar to that for the ^{4}He coated case [9, 19]. This suggests that the combination of a magnetic field and the surface solid ^{3}He may play a role in mediating the conversion from A* ⟶ B.

The superfluid transition, T_{ca}, occurs over a temperature band ~25 μK wide in accord with the heat capacity results of He *et al.* [26]. By carefully warming the sample from the B phase, we partially entered the T_{ca} band. After thermal equilibration and subsequent cooling at a rate of ~40 μK/h, we observed a trace that was intermediate between the pure A* and pure B phase. Thus, if the cell was warmed to a temperature within the T_{ca} band, the result was a partial conversion from the B ⟶ A* phases. We never initiated a partial or complete B ⟶ A* transition on warming unless we entered the T_{ca} band which we could approach to within 2 μK (see inset to Fig. 3) [27]. The evolution of the SM was very similar to that depicted in Fig. 3, indicating that only part of the ^{3}He B sample was converted back into A*. Different proportions of A* and B phase could be created depending on the depth of penetration into the T_{ca} or T_{A*B} bands. The pressure-independent widths of T_{ca} and T_{A*B} may be related to one another and due to inhomogeneities induced by compression of the ends of the aerogel during cell assembly. However, if the width were solely due to inhomogeneities and not pinning, we would expect the T_{A*B} width to diminish at high pressures, where the pressure dependence of T_{A*B} is weak (Fig. 2).

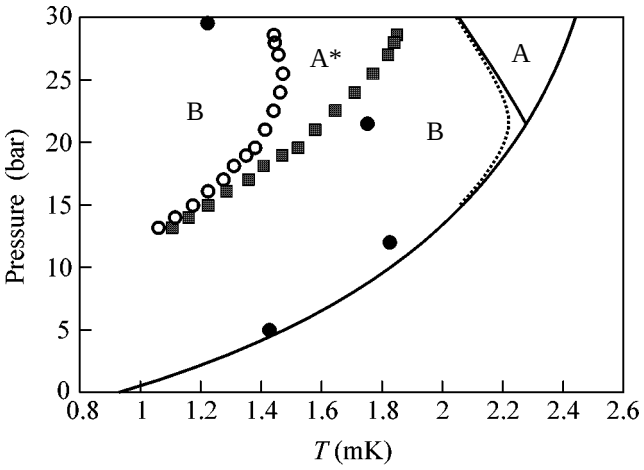

Fig. 2. The metastable ^{3}He A* phase in 98% open aerogel in zero magnetic field is bounded by squares that mark the onset of superfluidity (T_{ca}) and open circles that mark the A* ⟶ B transition observed while cooling. The symbols' width is comparable to the transitions' width. Solid lines show the bulk ^{3}He phase diagram in zero field, the dotted line shows the thermodynamically stable bulk B ⟶ A transition in a 24.9 mT field, and the A ⟶ B transitions observed in bulk ^{3}He in a specially prepared cell (filled circles) [25]. A similar (less pronounced) T_{A*B} suppression was seen at Northwestern [3].

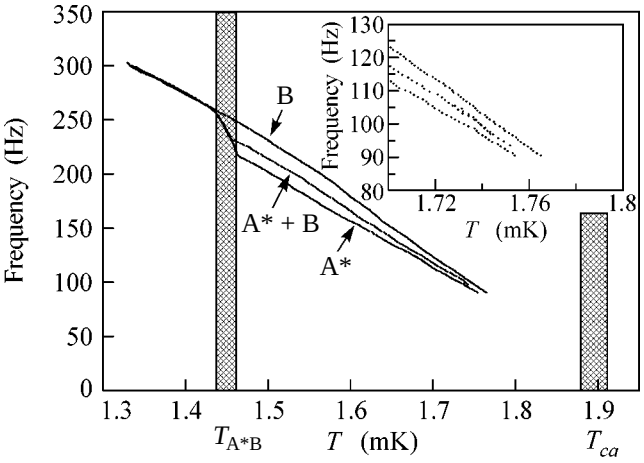

Fig. 3. The evolution of the peak frequency of the SM at 27.97 bar. The upper (warming) and lower (cooling) traces depict the B and A* phase results. The intermediate curve is a history-dependent trace obtained by initiating but not carrying to completion the A* ⟶ B transition. The inset shows a similar trace obtained by partial penetration into the T_{ca} band. The intermediate frequency SM is evidence for the stable coexistence of the A* and B phases of ^{3}He in 98% aerogel.

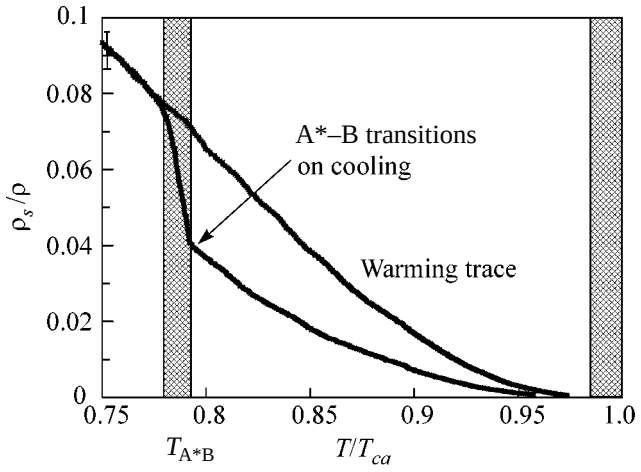

Fig. 4. Values of ρ_s/ρ in 98% aerogel at 27.97 bar. The upper curve shows data obtained in the B phase on warming. The lower curve was recorded on cooling; both were carried out at ~40 μK/h. The lower curve shows the signature of the A* ⟶ B transition. The cooling and warming traces overlap below the $T_{A^* \to B}$ "band."

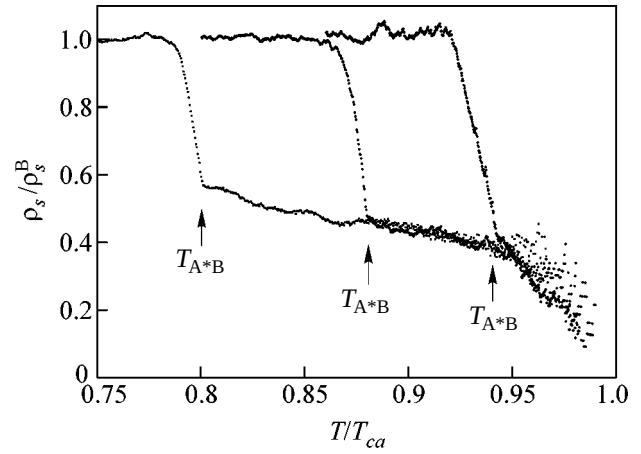

Fig. 5. The ρ_s/ρ_s^B ratio for P = 27.97, 22.53, and 16.05 bar (from left to right). Below T_{A*B} (once the transition is complete), only the B phase is present; thus, $\rho_s/\rho_s^B = 1$ (ρ_s^B is a function fitted to the B phase data obtained while warming).

Analysis of the velocity of the slow mode allows us to determine the superfluid fraction through the equation $\rho_s/\rho = \rho/\rho_a(c_s/c_a)^2$, where c_s is the slow mode velocity and c_a is the longitudinal sound velocity in aerogel. Using this equation, we calculate the ρ_s/ρ for the A* and B phases, after we subtract the frequency shift of the edge mode (described in Golov *et al.* [21]). The edge-mode velocity is $\sim(\rho_s^{bulk}/\rho)^{1/2}$ (ρ_s^{bulk} is the bulk ^{3}He superfluid fraction). In Fig. 4, we plot the ρ_s/ρ found for the A* and B phases at 28 bar. Errors due to the extrapolation of the edge-mode frequency shift ~±1% are comparable to the scatter in the data in Fig. 4.

The B-phase superfluid fraction ρ_s^B/ρ in Fig. 4 is similar to that measured by the torsional oscillator technique [5], while the supercooled A* data fall below. The superfluid density of the A* and B phases (28 bar, Fig. 4) is well fitted by the equation $\rho_s/\rho = A(1 - T/T_{ca})^b$. The (A, b) coefficients at 28, 22.53, and 16.05 bar are (1.2, 2.1), (1.4, 2.2), and (1.5, 3.5) and (0.83, 1.5), (1.5, 1.9), and (0.97, 2.1) for the A* and B phases, respectively. The higher exponent at 16.05 bar manifests the relatively rapid growth of ρ_s^{A*} near T_{ca} seen in Fig. 5 but is confined to a limited temperature range (Fig. 2). The ratio ρ_s^{A*}/ρ_s^B diminishes near T_{ca} (see Fig. 5), and the ratio $\rho_s^{A*}/\rho_s^B \le 0.5$ is smaller than that expected for bulk ^{3}He A even when **l** is oriented parallel to the superflow [28], a situation that is impractical to achieve due to wall orientation effects [29]. It is surprising that this strong suppression of ρ_s^{A*} is manifested in a medium with no preferred orientation and in the absence of a magnetic field, unless the A* phase gap is much smaller than that of the B phase.

The strong reduction of ρ_s^{A*} (and A* phase gap) compared to ρ_s^B raises the following question: Why is the A* phase so reproducibly initiated from the N state even in the presence of B phase within the aerogel and in the surrounding bulk fluid [4]? It is possible that the N state may transform more readily into A* rather than the pseudoisotropic B phase, or the region near T_{ca} may possibly contain precursor nonsuperfluid states [18, 30] that transform more readily into the A* phase.

In summary, the slow mode of ^{3}He in 98% aerogel in zero field was used to quantify the A* and B phase superfluid fractions, which differ by more than a factor of two, strongly implying that the A* and bulk A phases are distinct. We mapped the metastable A* ⟶ B transition in pressure and temperature. The A* phase persists with lifetimes greater than a day well below T_{ca} and can coexist on similar timescales with the B phase. We measure and quantify the width of the T_{A*B} and T_{ca} transitions. It is hoped that these measurements will spur theoretical efforts to understand the effects of disorder on the phase diagram.

J.M.P. acknowledges helpful conversations with I.A. Fomin, V.V. Dmitriev, T.L. Ho, and D. Einzel. Support was provided by the NSF (grant nos. DMR-0202113 and 9970817), by the CRDF, and by NATO under SA (grant no. (PST.CLG.979379)6993/FP).

REFERENCES

1. Y.-H. Li and T.-L. Ho, Phys. Rev. B **38**, 2362 (1988).
2. J. V. Porto and J. M. Parpia, Phys. Rev. B **59**, 14583 (1999).
3. G. Gervais, T. M. Haard, R. Nomura, *et al.*, Phys. Rev. Lett. **87**, 35701 (2001).
4. G. Gervais, K. Yawata, N. Mulders, *et al.*, Phys. Rev. B **66**, 054528 (2002).
5. J. V. Porto and J. M. Parpia, Phys. Rev. Lett. **74**, 4667 (1995).
6. D. T. Sprague, T. M. Haard, J. B. Kycia, *et al.*, Phys. Rev. Lett. **75**, 661 (1995).
7. G. Gervais, K. Yawata, and W. P. Halperin, Phys. Rev. Lett. **88**, 209602 (2002).
8. P. Brussaard, S. N. Fisher, A. M. Guenault, *et al.*, Phys. Rev. Lett. **86**, 4580 (2001).
9. B. I. Barker, Y. Lee, L. Polukhina, *et al.*, Phys. Rev. Lett. **85**, 2148 (2000).
10. H. Alles, J. J. Kaplinsky, P. S. Wootton, *et al.*, Phys. Rev. Lett. **83**, 1367 (1999).
11. S. N. Fisher, R. P. Haley, and G. R. Pickett, Phys. Rev. Lett. **88**, 209601 (2002).
12. M. Boukhny, G. L. Bullock, and B. S. Shivaram, Phys. Rev. Lett. **73**, 1707 (1994).
13. J. B. Kycia, J. I. Hong, M. J. Graf, *et al.*, Phys. Rev. B **58**, R603 (1998).
14. P. Sharma and J. A. Sauls, J. Low Temp. Phys. **125**, 115 (2001).
15. E. V. Thuneberg, S. K. Yip, M. Fogelström, and J. A. Sauls, Phys. Rev. Lett. **80**, 2861 (1998).
16. I. A. Fomin, Pis'ma Zh. Éksp. Teor. Fiz. **77**, 285 (2003) [JETP Lett. **77**, 240 (2003)].
17. I. A. Fomin, J. Low Temp. Phys. **134**, 769 (2004).
18. G. E. Volovik, Pis'ma Zh. Éksp. Teor. Fiz. **63**, 281 (1996) [JETP Lett. **63**, 301 (1996)].
19. V. V. Dmitriev, I. V. Kosarev, N. Mulders, *et al.*, Physica B (Amsterdam) **329–333**, 320 (2003).
20. K. Matsumoto, J. V. Porto, L. Pollack, *et al.*, Phys. Rev. Lett. **79**, 253 (1997).
21. A. Golov, D. A. Geller, J. M. Parpia, *et al.*, Phys. Rev. Lett. **82**, 3492 (1999).
22. E. Nazaretski, G. Lawes, D. M. Lee, *et al.*, J. Low Temp. Phys. **126**, 685 (2002).
23. L. D. Landau, J. Phys. (Moscow) **5**, 71 (1941).
24. M. J. McKenna, T. Slawecki, and J. D. Maynard, Phys. Rev. Lett. **66**, 1878 (1991).
25. P. Schiffer, M. T. O'Keefe, M. D. Hildreth, *et al.*, Phys. Rev. Lett. **69**, 120 (1992).
26. J. He, A. D. Corwin, J. M. Parpia, *et al.*, Phys. Rev. Lett. **89**, 115301 (2002).
27. The SM signal is extinguished within $0.98T/T_c$. However, if the sample is cooled after warming to within 2 μK of T_{ca}, we see no conversion into the A* phase.
28. S. Higashitani, J. Low Temp. Phys. **114**, 161 (1999).
29. J. E. Berthold, R. W. Giannetta, E. N. Smith, *et al.*, Phys. Rev. Lett. **37**, 1138 (1976).
30. Yu. M. Bunkov, A. S. Chen, D. J. Cousins, *et al.*, Phys. Rev. Lett. **85**, 3456 (2000).

JETP Letters, Vol. 79, No. 8, 2004, pp. 388–391. Translated from Pis'ma v Zhurnal Éksperimental'noĭ i Teoreticheskoĭ Fiziki, Vol. 79, No. 8, 2004, pp. 475–479.

Mechanism for the Appearance of a High-Efficiency Brownian Motor with Fluctuating Potential

V. M. Rozenbaum

Institute of Surface Chemistry, National Academy of Sciences of Ukraine, ul. Generala Naumova 17, Kiev, 03164 Ukraine
e-mail: vrozen@mail.kar.net

Received February 9, 2004; in final form, March 10, 2004

A version of a Brownian motor (system generating a unidirectional motion of a Brownian particle in an asymmetric fluctuating potential) is considered for the case where the potential consists of an asymmetric periodic component undergoing random shifts by a half-period L with a certain frequency and the potential of an external force F. The high efficiency of such a motor (ratio of the useful work against the load force F to the energy imparted to the particle due to the potential shifts) is due to a high and narrow barrier, as well as to a smooth arbitrarily shaped potential relief repeated with an energy shift on both half-periods L. Simple analytic expressions are obtained for the flux and efficiency as functions of the load force over a wide frequency range. © *2004 MAIK "Nauka/Interperiodica".*

PACS numbers: 05.40.Jc

Nonequilibrium fluctuations leading to the unidirectional motion of Brownian particles in asymmetric media even in the absence of an external field are of methodological and applied interest in connection with the study and design of so-called Brownian motors—"nanomotors" converting various types of energy into mechanical energy, systems segregating nanoparticles, molecular pumps driven by the splitting energy of adenosine triphosphate, etc. A number of models have been proposed for describing the ordered motion of particles in asymmetric potentials fluctuating due to external factors such as, e.g., chemical reactions [1–3].

As is known, Brownian motors are characterized by the flux J, determining the average velocity of unidirectional motion, and the efficiency η, characterizing the ratio of the useful work against an external load force F to the energy spent for potential fluctuations [3, 4]. Figure 1 shows the typical behavior of the functions $J(F)$ and $\eta(F)$. It is seen that a monotonic decrease in J upon an increase in load F and nonmonotonic behavior of $\eta(F)$ are characteristic of the Brownian motor, as well as of any motor. It was thought for some time that high efficiency is inherent only in adiabatic deterministic models for which η is close to unity in the limit of infinitely weak load ($F \longrightarrow 0$) and infinitely long period of potential variation ($T \longrightarrow \infty$), such that the product FT is finite [4]. In models with the instantaneous potential switching (e.g., in fast chemical reactions), which are most interesting for biological applications, η is limited by a value on the order of 0.05 [4]. This fact is explained either by the use of simple potentials with only a few varying parameters (e.g., sawtooth potentials characterized only by the amplitude and asymmetry parameter) to simplify calculations or by the absence of potential in one of the switching states, providing a purely diffusional stage of motion. To achieve higher efficiency in this class of models, the switching potentials must be identical and shifted by a half-period [5, 6]. Parmeggiani *et al.* [5] considered a sawtooth potential and assumed that a Brownian particle can move from this potential to its half-period-shifted copy only in the narrow vicinity of the potential minimum. A double-well periodic potential with the wells separated by a half-period and having high barriers between them, to allow the kinetic description of the Brownian particle hopping between wells in the case of a low

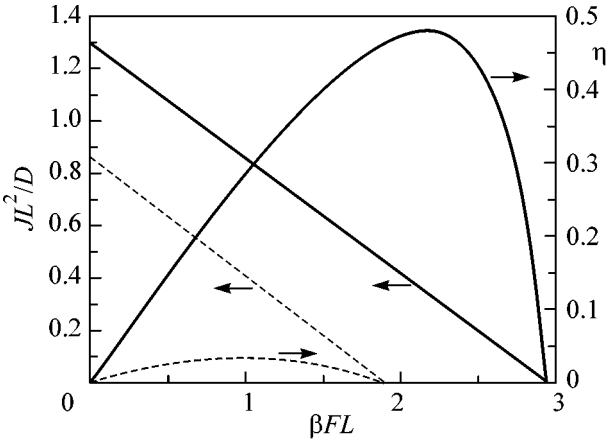

Fig. 1. (monotonically decreasing lines) Particle flux J and (nonmonotonic lines) efficiency η of the Brownian motor vs. the load force F in the (solid lines) presence and (dashed lines) absence of a high narrow barrier that locks the reverse flux and improves the characteristics of the motor. The parameters of the plots are given in the text.

0021-3640/04/7908-0388$26.00 © 2004 MAIK "Nauka/Interperiodica"

switching frequency, was studied in [6]. High efficiency was achieved if one barrier was much higher than the other.

In this work, a mechanism for the appearance of a high-efficiency Brownian motor is analyzed for a wide class of potentials $U(x) = V(x) + Fx$, where $V(x) = V(x + 2L)$ is the asymmetric component undergoing random shifts by a half-period L with frequency γ and F is the load force. The approach used below is as follows. The dynamics of Brownian particle motion in the potentials $U^{\pm}$ [superscripts + and – denote the potentials with components $V(x)$ shifted by a half-period and the related quantities] are determined by two distribution functions $\rho^{\pm}(x, t)$ satisfying the following Smoluchowski equation [7] with an additional term describing the random transitions of a particle between the potentials $U^{\pm}$ with frequency γ:

$$\frac{\partial \rho^{\pm}(x,t)}{\partial t} = -\frac{\partial j^{\pm}(x,t)}{\partial x} - \gamma[\rho^{\pm}(x,t) - \rho^{\mp}(x,t)]. \quad (1)$$

Here, the fluxes $j^{\pm}(x, t)$ are given by the expression

$$j^{\pm}(x,t) = -De^{-\beta U^{\pm}(x)}\frac{\partial}{\partial x}[e^{\beta U^{\pm}(x)}\rho^{\pm}(x,t)], \quad (2)$$

where D is the diffusion coefficient and $\beta = (k_B\tilde{T})^{-1}$ (k_B is the Boltzmann constant and $\tilde{T}$ is the absolute temperature). In the stationary state, the total flux is constant and can be represented in the form

$$J = 2j^{+}(0) + \gamma R(L), \quad R(x) \equiv \int_0^x [\rho^{-}(x') - \rho^{+}(x')]dx'. \quad (3)$$

Expression (3) is obtained by integrating Eq. (1) with respect to x under the conditions $\rho^{\pm}(x + L) = \rho^{\mp}(x)$ and $j^{\pm}(x + L) = j^{\mp}(x)$, which follow from the equality $V^{\pm}(x + L) = V^{\mp}(x)$. These conditions also determine the following expression for the energy expended for switching the potentials $U^{+} \longrightarrow U^{-} \longrightarrow U^{+}$ per unit time:

$$W_{\text{in}} = 2\gamma\int_0^L [V^{+}(x) - V^{-}(x)][\rho^{-}(x) - \rho^{+}(x)]dx. \quad (4)$$

Since the useful work done per unit time against the external load force F is equal to $W_{\text{out}} = 2FLJ$, Eqs. (3) and (4) determine the motor efficiency $\eta = W_{\text{out}}/W_{\text{in}}$. If the difference $\Delta V = V^{+}(x) - V^{-}(x)$ varies only slightly with x, then $W_{\text{in}} \approx 2\gamma\Delta V R(L)$ and

$$\eta \approx \frac{FL}{\Delta V}\left[1 + \frac{2j^{+}(0)}{\gamma R(L)}\right]. \quad (5)$$

The value of η tends to unity when $FL \longrightarrow \Delta V$, provided that the negative flux $j^{+}(x)$ is low at the point $x = 0$. The latter condition is fulfilled if the periodic component of the potential $V^{+}(x)$ includes a high barrier V_0 at the point $x = 0$. Thus, the efficiency of the Brownian motor is high if the following two conditions are simultaneously satisfied. First, a high narrow barrier V_0 exists that locks the reverse flux. Second, a smooth potential relief $v(x)$ of an arbitrary shape is repeated with the energy shift ΔV on both half-periods of the function $V^{+}(x)$.

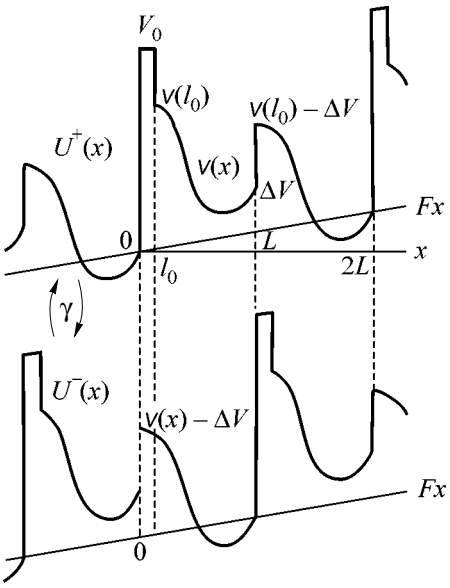

Fig. 2. Potentials $U^{\pm}(x) = V^{\pm}(x) + Fx$ including the asymmetric periodic components $V^{\pm}(x) = V^{\pm}(x + 2L) = V^{\mp}(x + L)$ shifted by a half-period L with frequency γ and the external load force field F. Each potential has a high barrier V_0 in a narrow range l_0. The smooth relief $v(x)$ is repeated on both half-periods L with the shift ΔV. The periodicity of the functions $V^{\pm}(x)$ is ensured by its jumps. The potential curves and limiting points on them are shown with respect to the Fx straight line.

Let us analyze the possibility that these conditions are satisfied simultaneously. Both these conditions are approximately satisfied for the double-well potential considered in [6]. Indeed, if the curvature of the potential at the extreme points is much larger than F/L, the positions of these points can be treated as independent of F. Since the wells are shifted from each other by a half-period L, the Brownian particle moves between the narrow vicinities of their minima upon potential switching. The shapes of other sections of the potential need not be identical. Therefore, it is easy to ensure the high barrier at the point $x = 0$ and satisfy the periodic boundary conditions.

In the case under consideration, where the function $v(x)$ is arbitrary, the above conditions are exactly met if the potentials $U^{\pm}$ change jumpwise near the points $x = 0$ and L (Fig. 2). Let us define the function $V^{+}(x)$ on two half-periods as

$$V^{+}(x) = \begin{cases} V_0, & 0 \le x < l_0, \\ v(x), & l_0 \le x < L, \end{cases} \quad (6)$$

$$V^{+}(x + L) = v(x) - \Delta V, \quad 0 \le x < L,$$

so that it has jumps V_0, $V_0 - \nu(l_0)$, and $\nu(l_0) - 2\Delta V$ at the points $x = 0$, l_0, and L, respectively [$\nu(L) = \Delta V$ according to the choice of the origin in Fig. 2]. In the limit $l_0 \longrightarrow 0$, the boundary conditions at the points $x = 0$ and L can easily be derived from Eq. (2). They include the conditions for flux continuity at these points and the relations

$$\Lambda j^+(0) = D[\rho^-(L) - e^{\beta\nu(l_0)}\rho^+(l_0)], \quad \Lambda \equiv l_0 e^{\beta V_0}, \quad (7)$$

$$\rho^+(L) = e^{\beta[\nu(l_0) - 2\Delta V]}\rho^-(l_0), \quad (8)$$

allowing for the equality $\rho^{\pm}(x + L) = \rho^{\mp}(x)$. In the same limit, Eq. (4) takes the form $W_{\text{in}} = 2\gamma\Delta V R(L)$, because it is assumed that $V_0 l_0 \longrightarrow 0$. In this case, arbitrary values of the parameter Λ are admissible. In particular, $\Lambda/L \gg 1$ can be taken.

It is convenient to introduce new variables $\xi_{1,2}(x) = \rho^+(x) \mp \rho^-(x)$, which, with allowance for Eqs. (1) and (2), satisfy the following differential equations in the interval $l_0 < x < L$:

$$\xi_1''(x) + \beta[\nu'(x) + F]\xi_1'(x) + [\beta\nu''(x) - 2\gamma/D]\xi_1(x) = 0, \quad (9)$$

$$\xi_2'(x) + \beta[\nu'(x) + F]\xi_2(x) = -J/D. \quad (10)$$

The general solution to Eq. (9) includes two arbitrary constants C_1 and C_2. Two arbitrary constants C_3 and J enter into the following general solution to Eq. (10):

$$\xi_2(x) = e^{-\beta[\nu(x) + Fx]}\left[C_3 - (J/D)\int_{l_0}^{x} e^{\beta[\nu(x') + Fx']}dx'\right]. \quad (11)$$

These four constants can be found from Eqs. (3), (7), and (8) [$j^+(0)$ and $R(L)$ are expressed in terms of the solutions to Eqs. (9) and (10)] and the normalization condition

$$\int_{l_0}^{L}\xi_2(x)dx = C_3 Z_- - (J/D)Z_{-+} = \frac{1}{2}, \quad (12)$$

where

$$Z_{\pm} \equiv \int_{l_0}^{L} e^{\pm\beta[\nu(x) + Fx]}dx,$$
$$Z_{-+} \equiv \int_{l_0}^{L} dx e^{-\beta[\nu(x) + Fx]}\int_{l_0}^{x} dx' e^{+\beta[\nu(x') + Fx']}. \quad (13)$$

It is difficult to implement the above solution procedure, because Eq. (9) with an arbitrary function $\nu(x)$ can be solved only numerically. However, the basic features of the model are revealed in the limiting cases: low, $\gamma\tau \ll 1$, and high, $\gamma\tau \gg 1$, frequencies γ of potential switching, where the characteristic time τ of establishing equilibrium in the smooth potential relief $\nu(x) + Fx$ is estimated as $\tau = Z_+ Z_-/2D \geq L^2/2D$.

For $\gamma\tau \ll 1$, the solution $\xi_1(x)$ to Eq. (9) is approximated by Eq. (11) with the change of constants C_3 and $-J/D$ to C_1 and C_2, respectively. In this case, the quantities $j^+(0)$ and $R(L)$ entering into the expressions for the main motor characteristics [see Eqs. (3) and (5)] take the form

$$j^+(0) = -\frac{\sinh\beta FL}{S},$$

$$R(L) = \frac{\Lambda Z_-(e^{\beta\Delta V} - e^{\beta FL}) + 2Z_+ Z_- \sinh\beta\Delta V}{2S}, \quad (14)$$

$$S = \Lambda Z_-(e^{\beta\Delta V} + e^{\beta FL}) + 2Z_+ Z_-(\cosh\beta\Delta V + e^{-\beta FL}) + 4Z_{-+}\sinh\beta FL.$$

It is significant that the quantity $R(L)$ responsible for the generation of unidirectional motion is independent of the diffusion coefficient D and is positive for $FL < \Delta V$ [$R(L)$ changes sign at $F = F_0$, where $F_0 L \longrightarrow \infty$ as $\Lambda \longrightarrow 0$ and $F_0 L \longrightarrow \Delta V$ as $\Lambda \longrightarrow \infty$]. In turn, the flux $j^+(0)$ is proportional to D, is negative for $F > 0$, and decreases monotonically with increasing F. Therefore, $J = 0$ at the stop point $F = F_s$ satisfying the inequality $F_s L < \Delta V$ ($F_s \longrightarrow \Delta V$ as $\Lambda \longrightarrow \infty$). From Eqs. (5) and (14), it follows that the efficiency at $\Lambda = 0$ is expressed as

$$\eta = \frac{FL}{\Delta V}\left(1 - \frac{1}{\gamma\tau}\frac{\sinh\beta FL}{\sinh\beta\Delta V}\right) \quad (15)$$

and its maximum η_m is small in the parameter $\gamma\tau \ll 1$. At $\Lambda \longrightarrow \infty$ one has: $j^+(0) \longrightarrow 0$, the quantity $R(L) \longrightarrow (1/2)\tanh\beta(\Delta V - FL)/2$ is independent of the function $\nu(x)$, and η is a linear function of $FL/\Delta V$ [see Eq. (5)]. Analysis of the behavior of the function $\eta(F)$ at $FL \longrightarrow \Delta V$ requires the inclusion of corrections small in the parameter

$$\varepsilon \equiv \frac{Z_+}{\Lambda}\frac{1 - \exp(-2\beta\Delta V)}{\beta\Delta V} \ll 1. \quad (16)$$

Then, to the terms of order ε, we obtain

$$\eta = \frac{FL}{\Delta V}\frac{F_s - F}{F_0 - F}, \quad F_0 L = \Delta V(1 + \varepsilon),$$
$$F_s L = \Delta V\left(1 + \varepsilon - \frac{\varepsilon}{\gamma\tau}\right), \quad \varepsilon \ll \gamma\tau \ll 1. \quad (17)$$

The maximal value $\eta_m(F_m)$ is determined by the expressions

$$\eta_m = (1+\varepsilon)\left[1-\sqrt{\frac{\varepsilon}{\gamma\tau(1+\varepsilon)}}\right]^2,$$
$$F_m L = \Delta V(1+\varepsilon)\left[1-\sqrt{\frac{\varepsilon}{\gamma\tau(1+\varepsilon)}}\right], \quad (18)$$

which explain the mechanism of appearance of a high-efficiency motor. The limiting behavior $\eta_m \longrightarrow 1$ is realized in the frequency range $\varepsilon \ll \gamma\tau \ll 1$, i.e., when the average lifetime γ^{-1} of the potentials $U^{\pm}$ is sufficiently long for establishing equilibrium in the smooth potential relief $v(x) + Fx(\gamma^{-1} \gg \tau)$ but is insufficient for the particle to overcome high narrow barriers $V_0(\gamma^{-1} \ll \tau/\varepsilon)$. For this reason, the reverse flux is locked, which ensures the near-unity value of η for the load force F that approximately compensates the shift ΔV of the smooth reliefs $v(x)$ (see Fig. 2 for $FL \approx \Delta V$). The identity of the smooth reliefs on both half-periods at $\Lambda \longrightarrow \infty$ and $FL \approx \Delta V$ leads to the relations $\rho^-(x) = \rho^+(x)\exp\beta(\Delta V - FL) \approx \rho^+(x)$, which makes it possible to exclude the energy losses associated with relaxation after switching the potentials.

For $\gamma\tau \gg 1$, the partial solutions to Eqs. (9) are approximated by the functions $\exp(\pm\sqrt{2\tilde{\gamma}}x)$, where $\tilde{\gamma} \equiv \gamma/D$. In this case, the main characteristics of the motor under the stronger inequality $\tilde{\gamma}L^2 \gg 1$ take the form

$$j^+(0) = \frac{D}{4S}(A - 2\sqrt{2\tilde{\gamma}}Z_+ e^{-\beta FL}\sinh\beta\Delta V),$$
$$R(L) = \frac{1}{\sqrt{2\tilde{\gamma}}S}$$
$$\times[\Lambda(e^{\beta\Delta V-\beta FL}-1) + 2Z_+ e^{-\beta FL}\sinh\beta\Delta V],$$
$$J = \frac{D}{2S}[\sqrt{2\tilde{\gamma}}\Lambda(e^{\beta\Delta V-\beta FL}-1) + A],$$
$$S = \sqrt{2\tilde{\gamma}}\Lambda[Z_+Z_-e^{\beta\Delta V-\beta FL} - Z_{-+}(e^{\beta\Delta V-\beta FL}-1)] \quad (19)$$
$$+ \Lambda Z_-(e^{2\beta\Delta V} + e^{\beta v(l_0)})$$
$$+ 2Z_+Z_-e^{-\beta FL}(e^{\beta\Delta V} + e^{\beta v(l_0)}\cosh\beta\Delta V) - Z_{-+}A,$$
$$A = 2e^{\beta v(l_0)}(e^{-\beta FL}\cosh\beta\Delta V - 1)$$
$$+ 2e^{\beta\Delta V-\beta FL} - 1 - e^{2\beta\Delta V}.$$

For $\Lambda = 0$, the absolute values of $j^+(0)$ and $\gamma R(L)$ are large in the parameter $\sqrt{\tilde{\gamma}}Z_+$, and the terms proportional to this parameter are cancelled in the expression for J. Therefore, efficiency is again low, though in the parameter $(\sqrt{\tilde{\gamma}}Z_+)^{-1}$. In the case $\Lambda \longrightarrow \infty$ of interest, $j^+(0) \longrightarrow 0$ and $J \longrightarrow \gamma R(L)$ [$\gamma R(L)$ is independent of γ]. At $FL \longrightarrow \Delta V$, η and η_m are given by Eqs. (17) and (18), respectively, with $\gamma\tau = 1$. Then, the maximal possible efficiency is generally estimated as

$$\eta_m \sim 1 - \sqrt{L/l_0}\exp(-\beta V_0/2). \quad (20)$$

Figure 1 illustrates a strong increase in the efficiency η in the presence of a high narrow barrier (cf. the solid and dashed lines with the right arrows). The functions $J(F)$ and $\eta(F)$ are calculated by Eqs. (5), (13), and (19) for the extremely asymmetric sawtooth potential $v(x) = v(l_0)(1 - x/2L)$ with $v(l_0) = 2\Delta V(l_0 \longrightarrow 0)$ for $\beta\Delta V = 3$ and $\gamma L^2/D = 100$. The solid and dashed lines correspond to the values $\Lambda/L = 1000$ and 0, respectively.

In conclusion, we note that the flux J for $F = 0$ in the above model tends to a nonzero constant at $\gamma \longrightarrow \infty$. At first glance, this behavior contradicts the known behavior $J \longrightarrow 0$ at $\gamma \longrightarrow \infty$ (see, e.g., [1]). However, the latter behavior is characteristic of the potentials without jump changes. If a sharp change in the potential by the value V occurs in the finite interval l, the boundary conditions specified by Eqs. (7) and (8) (as well as all above results) are valid if $\gamma \ll D(\beta V/l)^2$. For $l \neq 0$, there is the range of very high frequencies $\gamma \gg D(\beta V/l)^2$, where the average lifetime γ^{-1} of the potentials $U^{\pm}$ is insufficient for a particle to cover the section l. In this region, the particle flux is insensitive to the shape of potential relief and tends to zero as $\gamma \longrightarrow \infty$, according to the above behavior.

I am grateful to Yu.A. Makhnovskiĭ for stimulating discussions.

REFERENCES

1. P. Reimann, Phys. Rep. **361**, 57 (2002).
2. R. D. Astumian, Science **276**, 917 (1997).
3. F. Jülicher, A. Ajdari, and J. Prost, Rev. Mod. Phys. **69**, 1269 (1997).
4. J. M. R. Parrondo, J. M. Blanko, F. J. Chao, and R. Brito, Europhys. Lett. **43**, 248 (1998).
5. A. Parmeggiani, F. Jülicher, A. Ajdari, and J. Prost, Phys. Rev. E **60**, 2127 (1999).
6. Yu. A. Makhnovskii, V. M. Rozenbaum, D.-Y. Yang, *et al.*, Phys. Rev. E **69**, 021102 (2004).
7. H. Riskin, *The Fokker-Plank Equation, Methods of Solutions and Applications* (Springer, Berlin, 1989).

Translated by R. Tyapaev